Astronomy & Astrophysics manuscript no. aa58834-25corr
May 11, 2026

A changing-look Seyfert discovered by eROSITA reveals a two-component broad-line region

Alex Markowitz[1], Mirko Krumpe[2], David Homan[2,3], Bożena Czerny[4], Mariusz Gromazdki[5], Hartmut Winkler[6], Joern Wilms[7], Steven Hämmerich[7], Georg Lamer[2], Tathagata Saha[1,8], David A.H. Buckley[9,10,11], Malte Schramm[12], Daniel E. Reichart[13], Mara Salvato[14], Pietro Baldini[14]

[1]Nicolaus Copernicus Astronomical Center, Polish Academy of Sciences, ul. Bartycka 18, 00-716 Warsaw, Poland
[2]Leibniz-Institut für Astrophysik Potsdam (AIP), An der Sternwarte 16, 14482 Potsdam, Germany
[3]Institute of Astronomy, University of Cambridge, Madingley Road, Cambridge, CB3 0HA, United Kingdom
[4]Center for Theoretical Physics, Polish Academy of Sciences, Al. Lotników 32/46, 02-668, Warsaw, Poland
[5]Astronomical Observatory, University of Warsaw, Al. Ujazdowskie 4, 00-478 Warsaw, Poland
[6]Department of Physics, University of Johannesburg, PO Box 524, Auckland Park 2006, South Africa
[7]Dr. Karl Remeis-Observatory and Erlangen Centre for Astroparticle Physics, Friedrich-Alexander Universität Erlangen-Nürnberg, Sternwartstr. 7, 96049 Bamberg, Germany
[8]Inter-University Centre for Astronomy and Astrophysics, Post Bag 4, Ganeshkhind, Pune University Campus, Pune 411007, India
[9]South African Astronomical Observatory, PO Box 9, Observatory, Cape Town 7935, South Africa
[10]Department of Astronomy, University of Cape Town, Private Bag X3, Rondebosch 7701, South Africa
[11]Department of Physics, University of the Free State, PO Box 339, Bloemfontein 9300, South Africa
[12]Universität Potsdam, Karl-Liebknecht-Str. 24/25, 14476 Potsdam, Germany
[13]Department of Physics and Astronomy, University of North Carolina at Chapel Hill, Campus Box 3255, Chapel Hill, NC 27599-3255, USA
[14]Max-Planck-Institut für Extraterrestrische Physik, Giessenbachstr. 1, 85748 Garching, Germany

Received December 31, 2025; accepted April 14, 2026

ABSTRACT

Context. Extreme sudden changes in the flow of accreting gas onto supermassive black holes manifest themselves via large-amplitude multiband continuum variability, as well as changes to broad Balmer emission profiles, driving changing-look active galactic nuclei (AGN).
Aims. X-ray flux monitoring with Spectrum Roentgen Gamma (SRG)/eROSITA revealed that in the Seyfert AGN HE 1237−2252 the soft X-ray flux dipped abruptly, by a factor of 17 within 18 months. We initiated a follow-up campaign that caught the luminosity recovery after the dip, and enabled us to study how the various accretion components, including the broad-line region (BLR) and X-ray-emitting coronae, responded during this flux recovery.
Methods. Our campaign included multiband photometry, X-ray spectroscopy, and optical spectroscopy. We tracked as the accretion rate relative to Eddington increased by a factor of 7 in 3 years.
Results. Based on broad Hβ variability, HE 1237−2252 was subtype 1.0–1.2 in 2002, transitioned to subtype 1.8 by the time of the luminosity dip, and then transitioned back to subtype 1.0 within 3 months as luminosity recovered. Both transitions saw broad Hβ integrated line flux change by factors of 4–6. The broad Balmer profile is decomposed into a broad Gaussian consistent with virialized gas at 27±3 lt-dy, plus a double-peaked profile, consistent with a diskline structure at ≳5 lt-dy. The diskline component's relative contribution to the total profile increases as continuum flux rises.
Conclusions. The lack of significant obscuration in the X-ray spectra, as well as the IR continuum dip, point to an intrinsic pause in the accretion rate as opposed to variable line-of-sight obscuration. Candidates for the underlying mechanisms include propagating cold and warm fronts in the accretion disk. The increased prominence of the diskline BLR component's emission could be due to evolution in the physical extent of the X-ray corona, and in the fraction of >13.6 eV photons intercepted by the diskline, as the accretion rate increases.

Key words. galaxies: active – galaxies: Seyfert – X-rays: galaxies – individual objects: HE 1237−2252

1. Introduction

Active galactic nuclei (AGN) are powered by accretion of matter onto a supermassive black hole (Sołtan 1982) usually through an accretion disk that feeds the black hole. Accretion is stochastically variable on a wide range of timescales. Accretion episodes can be intermittent, with the global supply of gas supplied by the host galaxy turning on and off, likely on timescales of the order of 10^4 – 10^5 years (Schawinski et al. 2015; Shen 2021). In addition, during episodes of persistent accretion, AGN emission varies stochastically on timescales from hours to decades across the electromagnetic spectrum (e.g., Mushotzky et al. 1993).

In recent years, the community has been accumulating evidence for events where AGN undergo major changes in their accretion rates on timescales ranging from months to several years. Specifically, such events are thought to be a driver behind observations of changes in a given source's optical spectral

type, changing-look AGN (CLAGN; e.g., Tohline & Osterbrock (1976), Shappee et al. 2014, Denney et al. 2014, and LaMassa et al. 2015, to list just a few early examples).

Broadly, Seyfert and quasar AGN are classified as type 1 or type 2 based on their optical line emission properties (Khachikian & Weedman 1974). Both types exhibit narrow (several hundred km s^{-1}) emission lines emanating from the narrow-line region (NLR), but only type 1 galaxies additionally exhibit Doppler-broadened (several thousand km s^{-1}) emission lines emanating from the broad-line region (BLR). Intermediate classification types (1.2, 1.5, 1.8, 1.9) can be assigned depending on the strength of the broad Hβ component relative to the narrow Hβ component (Osterbrock & Koski 1976; Osterbrock 1977, 1981; Cohen 1983; Runco et al. 2016) or to [O III] λ5007 (Winkler 1992), and on the relative intensities of broad Hβ and broad Hα. For example, in type 1.8, broad Hα is detected well, while broad Hβ is detected but weakly; in type 1.9 broad Hβ is not detected, only broad Hα, while in type 2 galaxies neither Hα nor Hβ display broad components.

For a given CLAGN, observations of optical spectral type changes are often associated with observations of major concurrent changes in continuum flux (e.g., Denney et al. 2014; McElroy et al. 2016). Major changes in accretion rate are a natural explanation: the ionizing luminosity responds accordingly, driving changes in the illumination and ionization in the BLR (e.g., Korista & Goad 2000; Wu et al. 2023), and the optical spectral type thus evolves. However, the nature of these major changes in accretion rate is unclear; they could be due to changes in the rate of global accretion onto the disk, for example cold chaotic accretion (Gaspari et al. 2013). Alternately, they could be associated with locally operating instabilities in the accretion flow, such as a radiation pressure-induced instability (e.g., Lightman & Eardley 1974; Saxton et al. 2015; Śniegowska et al. 2023), or magnetically driven instabilities (Stern et al. 2018; Scepi et al. 2021). CLAGN events can also be triggered by stream-like accretion from tidal disruption events (TDEs) occurring in AGN, (e.g., Homan et al. 2023), including cases where a TDE-like stream is suspected of directly impacting the disk and corona (Ricci et al. 2020).[1]

Another open question is whether the BLR is a static reservoir of gas, passively getting illuminated by the disk and/or the corona, and then reradiating line emission. Alternatively, the BLR may be a wind outflowing from the disk, and it forms or dissipates when the accretion rate relative to Eddington, $\dot{m}_{\rm Edd} \equiv L_{\rm Bol}/L_{\rm Edd}$, transitions across a certain critical value (Elitzur & Ho 2009). Recent results for CL events support this notion, as CL quasars tend to accrete near such a critical value of accretion rate (Green et al. 2022; Panda & Śniegowska 2024). Meanwhile, samples of (non-CL) Seyferts and quasars suggest that type 2 galaxies are more prominent toward lower luminosities, possibly due to a decrease in the covering fraction of BLR clouds toward lower luminosities (Elitzur et al. 2014). Alternately, the BLR in type 2 galaxies may become more obscured toward lower luminosities due to an increase in the covering fraction of the obscuring torus (Ricci et al. 2017).

Changing-look AGN events occur rarely on a per-object basis, so monitoring a starting sample of AGN and quasars that is as large as possible is key for the detection of new CL events. Well over 150 CLAGN have been detected from repeat optical spectroscopy, for example the Time Domain Spectroscopic Survey within the Sloan Digital Sky Survey (SDSS) (Runnoe et al. 2016; Green et al. 2022; Zeltyn et al. 2024), and with additional forthcoming detections expected from large spectroscopic surveys such as the Dark Energy Spectroscopic Instrument (DESI) survey. Dozens more events have been identified via photometric monitoring using large-area (observed-frame) optical surveys such as the Zwicky Transient Facility, Catalina Real-time Transient Survey, and PanSTARRS (Yang et al. 2018; MacLeod et al. 2019; Ross et al. 2020; Frederick et al. 2021; López-Navas et al. 2022; Wang et al. 2024); mid-IR monitoring (Sheng et al. 2020); or combinations of wavelengths (López-Navas et al. 2023; Yang et al. 2025). Here one looks for large rapid changes in flux in excess of the amplitudes of variability associated with persistent accretion (e.g., Graham et al. 2020) or sudden strong deviations from the standard variability behavior associated with non-CLAGN, for example CLAGN straying from a damped random walk behavior (Suberlak et al. 2021; Sánchez-Sáez et al. 2021). In all cases, though, multiwavelength follow-ups while transitions are occurring are key to best exploring how accretion flow components — disk, X-ray corona, BLR — interact with each other during such major changes in accretion and luminosity.

In this paper we report the detection of a CLAGN using the X-ray band, specifically using the Extended ROentgen Survey with an Imaging Telescope Array (eROSITA; Predehl et al. 2021), the soft X-ray telescope on board the *Spectrum Roentgen/Gamma* (*SRG*) spacecraft (Sunyaev et al. 2021). From Decembeer 2019 to February 2022, eROSITA's all-sky surveys enabled X-ray monitoring on the order of a million AGN and quasars, once every six months, thus amplifying small numbers of rare transient AGN events, and providing the first X-ray-based channel for the identification of major changes in luminosity. Our team monitored AGN for major changes in soft X-ray flux, and in January 2022, we identified a Sy 1.0–1.2 (type based on archival spectra) whose soft X-ray flux had dropped by a factor of roughly 17 in 1.5 yr. We thus triggered target-of-opportunity observations encompassing X-ray spectroscopy and photometry, space-based UV/optical photometry, and ground-based optical photometry and spectroscopy, spanning from late 2022 through early 2025. As demonstrated below, by early 2022 the optical spectrum had transitioned into a subtype 1.8. Over the next year, the X-ray continuum recovered and the optical/UV continuum rose steadily; concurrently, the optical spectrum had transitioned back into a type 1 by June–August 2022. Then, during 2023–2024, the broad Balmer line profile evolved from being dominated by a single broad Gaussian-like component into a Gaussian plus a double-peaked structure.

The remainder of this paper is organized as follows. Section 2 describes the event detection and gives an overview of multiwavelength campaign. Section 3 gives an overview of the multiwavelength continuum variability. Sections 4, 5, and 6 describe, respectively, the X-ray spectral fits, the broadband spectral energy distribution (SED) modeling, and the fits to optical emission-line spectra. The results are discussed in Sect. 7, and we provide our summary and conclusions in Sect. 8.

Throughout this paper, we assume the cosmological parameters of $H_0 = 70$ km s^{-1} Mpc^{-1}, $\Omega_{\rm M} = 0.29$, and $\Omega_{\rm vac} = 0.71$. The redshift of J1240–2309 thus corresponds to a luminosity distance of 443 Mpc and a co-moving (proper) distance of 404 Mpc, using Ned Wright's Cosmology Calculator (Wright 2006).[2]

[1] In this paper, we do not discuss optical type change attributed to transit of a dusty cloud or wind across the line of sight (e.g., Goodrich 1995; Wang et al. 2009; Gaskell & Harrington 2018; Zeltyn et al. 2022); such events have been observed only very rarely.

[2] http://www.astro.ucla.edu/~wright/CosmoCalc.html

2. Counterpart, follow-up observations, and data reduction

2.1. Detection of the event in eROSITA scans

The position of the event was scanned in each of the five eROSITA All-Sky Surveys (eRASS; Merloni et al. 2024), hereafter referred to as eRASS1 to eRASS5. Every six months (every eRASS), a given position near the orbital equator is scanned six times at a four-hour cadence, each with a roughly 40 second exposure. These exposures are added to yield one flux point per eRASS. After eRASS5 scanned the position of the point source in question, we detected an extreme flux drop from eRASS2 to eRASS5. We identified the event with the eROSITA DR1 (Merloni et al. 2024) source 1eRASS J124028.2−230925. The error of the DR1 position in each coordinate, as given in catalogue column POS_ERR, is 1.″2.[3] We cross-matched with known AGN and quasar catalogs (Salvato et al. 2025) to identify the counterpart. The closest counterpart is the Seyfert HE 1237−2252, identified in the Hamburg/ESO survey by Reimers et al. (1996), and located 1.″6 from the X-ray position,[4] at J2000 coordinates $\alpha = 12^{h}40^{m}28\overset{s}{.}32$, $\delta = -23°09'26\overset{''}{.}7$. It is also cross-listed as the IR source WISEA J124028.32−230926.7 and 6dF J1240283−230927; the event is thus referred to hereafter as J1240–2309.[5] Its redshift z is 0.09643±0.00015 (6dF Galaxy Survey; Jones et al. 2009; see also Reimers et al. 1996).

We conducted spectral fits for each individual eRASS scan, as described in Sect. 4.2. We determined that J1240–2309's 0.5–2.0 keV flux had decreased by a factor of $17.0^{+16.3}_{-7.2}$ over 18 months, from $9.32^{+1.01}_{-1.26} \times 10^{-13}$ erg cm^{-2} s^{-1}in eRASS2 (June 2020) to $5.5^{+2.7}_{-2.4} \times 10^{-14}$ erg cm^{-2} s^{-1}in eRASS5 (January 2022). The start and stop times of the scans that included the position of J1240–2309 are listed in Table A.1. For brevity, all details of eROSITA data reduction, including source and background spectral extraction, and soft X-ray flux measurements are detailed in Appendix B.1. Good exposure times after correcting for vignetting effects were in the range 230–280 s, as listed in Table A.1.

2.2. Multiwavelength campaign overview

Following the identification in January 2022 of the major change in soft X-ray flux in J1240–2309, we triggered multiple target-of-opportunity observations as follows:

We obtained a high signal-to-noise X-ray spectrum with the *XMM-Newton* (Jansen et al. 2001) European Photon Imaging Cameras (EPIC; Strüder et al. 2001) in January 2022 (hereafter XM1). *XMM-Newton*'s Optical Monitor (OM; Mason et al. 2001) also provided a concurrent set of optical/UV photometry points.

In February 2022, the eRASS scans were suspended, so we supplemented the X-ray flux monitoring with *Neil Gehrels Swift Observatory* (*Swift*; Gehrels et al. 2004) X-Ray Telescope (XRT; Burrows et al. 2005) monitoring, consisting of 15 pointings between February 2022 and August 2024, hereafter referred to as Sw1–15. These observations also provided optical and UV photometric monitoring courtesy of *Swift*'s UltraViolet/Optical Telescope (UVOT). We also included X-ray fluxes from a 2013 *XMM-Newton* slew, obtained via the *XMM-Newton* Upper Limit Server.[6]

Meanwhile, we obtained B-, V-, R-, and I-band photometry at ground-based facilities operated by the Las Cumbres Observatory global telescope (LCOGT; Brown et al. 2013) network, with nine observations obtained between 1 March 2022 and 24 May 2023 (LCO1–9), as listed in Table A.2. We also obtained 13 B-, V-, and/or R-band photometric observations of J1240–2309 between 7 February 2022 and 7 May 2022 using the 0.4-meter PROMPT6 telescope at Cerro Tololo Inter-American Observatory, operated as part of the Skynet Robotic Telescope Network. They are also listed in Table A.2.

The dates, ObsIDs, and exposures for all X-ray observations are given in Table A.1. The dates, filters, and exposures for all optical/UV photometric observations are given in Table A.2.

To track the behavior of the Balmer emission line profiles, we conducted optical spectroscopic monitoring, using the South African Large Telescope (SALT) longslit Robert Stobie Spectrograph (RSS; Burgh et al. 2003; Kobulnicky et al. 2003), the FORS2 spectrograph (Appenzeller et al. 1998) on the 8.2 m Very Large Telescope Array's (VLT) UT1 at Cerro Paranal, and the SpUpNIC spectrograph (Crause et al. 2019) at the South African Astronomical Observatory (SAAO) 1.9 m telescope. We obtained a total of 19 new observations of J1240–2309 between February 2022 and December 2024, hereafter referred to as spectra #3–21. Spectra #1 and #2 refer to archival spectra taken in 1993 at the ESO 3.6 m telescope as part of the Hamburg/ESO (H/ESO) survey (Reimers et al. 1996) and in 2002 at the UK Schmidt Telescope as part of 6dFGS (Jones et al. 2009), respectively. The dates, instruments, and exposures for all spectra are listed in Table A.3.

Throughout 2022, both X-ray and optical/UV fluxes rose quasi-steadily. By December 2022, $F_{0.5-2.0}$ had risen back to $11.8^{+1.3}_{-1.1} \times 10^{-13}$ erg cm^{-2} s^{-1}; the far-UV flux (UVW1, UVM2, UVW2 filters) had concurrently increased by factors spanning 1.5–2.0 compared to fluxes in January 2022. We thus triggered a second *XMM-Newton* observation, which was executed in January 2023 (XM2), followed by additional *Swift* pointings through August 2024, as well as 28 visits with the Neutron Star Interior Composition Explorer (NICER; Gendreau et al. 2016) aboard the International Space Station, between 15 February 2023 and 23 May 2023. We conducted a third *XMM-Newton* observation in January 2025 (XM3).

Finally, we supplemented these data with publicly available optical and infrared photometry. We used data taken with the Asteroid Terrestrial impact Last Alert System (ATLAS) during November 2017 – December 2023 and with the *Widefield Infrared Survey Explorer* (*WISE*)/*NEOWISE* during January 2012 – June 2023, respectively.

For brevity, further details of observations (e.g., the gratings used for optical spectroscopy), as well as all details of data reduction, calibration, and extraction of all X-ray spectra and photometric fluxes can be found in the Appendices, and the resulting X-ray fluxes and optical, UV, and IR magnitudes are given in tabular form in the Appendices as follows: B.1: eROSITA; B.2: *XMM-Newton* EPIC; B.3: *Swift* XRT; B.4: NICER; B.5: *XMM-Newton* OM; B.6: *Swift* UVOT; B.7: LCOGT; B.8: PROMPT-

[3] Includes statistical and systematic uncertainties corresponding to the 1σ confidence interval given the R.A. and Dec. for this source.

[4] After J1240–2309, the next closest counterpart candidates listed in NED are all ≥ 29″ away.

[5] While the offset between the X-ray position and position of this counterpart is slightly larger than the nominal X-ray position center, counterpart identification is not affected. In addition, as demonstrated below, X-ray fluxes determined from times outside the flux dip – eRASS1 and eRASS2 in 2019–2020, an *XMM-Newton* slew in 2013, and our *Swift* and *XMM-Newton* points from the end of our campaign – are all in reasonable agreement with each other.

[6] http://xmmuls.esac.esa.int/upperlimitserver/

6; B.9: ATLAS and *WISE/NEOWISE*; and B.10: SALT, VLT, & SAAO 1.9m optical spectra.

3. Multiband continuum variability overview

The IR flux remained relatively steady from 2010 until 2019 (Fig. B.1), indicating a relatively stable bolometric output during this period. Meanwhile, the archival 0.5–2 keV flux from the 2013 *XMM-Newton* slew was $(1.53 \pm 0.44) \times 10^{-12}$ erg cm^{-2} s^{-1}, with fluxes in 2019–2020 (eR1, eR2; discussed in Sect. 4.2) only a factor of 1.6 lower.[7]

However, as shown in Fig. 1 and Fig. B.1, from mid-2019 until late 2021, the IR flux dropped by roughly 0.7 mag in both W1 and W2 bands. This change is similar to the average change in magnitudes (ΔW1 = 0.65; ΔW2 = 0.88) displayed by the ten optically confirmed CLAGN with strong mid-IR variability identified by Sheng et al. (2017). Meanwhile, as illustrated in Fig. 1, the 0.5–2 keV X-ray flux decreased steadily from 2020 through early 2022, when we triggered the optical/UV photometric monitoring.

After early 2022, all bands increased steadily through late 2022: $F_{0.5-2.0}$, far-UV (UVW1 and UVM2) flux, and IR (W1) flux saw increases by factors of roughly 26, 2.5–3.0, and 1.5 from January 2022 through December 2022. Then, starting in early 2023, the X-ray flux became rather stable, and varied only minimally for the next two years; values of $F_{0.5-2.0}$ have varied by 37 percent (fractional variability amplitude), and have typically remained in the range 0.8–2.2 $\times 10^{-12}$ erg cm^{-2} s^{-1}, consistent with the fluxes measured in 2013 and 2019–2020. Since mid-2023, the far-UV fluxes have also become overall stable, varying by only 23–28%. Meanwhile, from 2020 through mid-2024, IR flux recovered by roughly 0.4–0.5 mag in both bands. Throughout the flux drop and recovery, the W1−W2 color remained steady at 0.7–0.8 (Fig. B.1), suggesting that AGN activity has remained persistent, following Stern et al. (2012) and Assef et al. (2018). Importantly, the dip in the *WISE/NEOWISE* light curve effectively excludes that the variability in the UV/X-ray bands can be attributed to obscuration by a cloud along the line of sight.

We performed cross-correlations on selected pairs of light curves, using the interpolated correlation function (ICF; White & Peterson 1994) with bootstrap errors determined by flux randomization (Peterson et al. 1998), due to the limited number of data points. All pairs of data points are generally well correlated at zero lag, with zero-lag correlation coefficients of 0.67–0.78 for $F_{0.5-2.0}$ to the IR bands; 0.67–0.79 for $F_{0.5-2.0}$ to the U, UVW1, UVM2, and UVW2 bands; 0.85–0.97 for comparisons of U, UVW1, UVM2, and UVW2 to each other; and 0.64–0.88 for U, UVW1, UVM2, and UVW2 to the IR bands. The data do not yield any evidence of lags or leads. For instance, we find an upper limit of ±360 days for any lag from $F_{0.5-2.0}$ to *WISE/NEOWISE* W1. Similarly, the best-fitting values for the *WISE/NEOWISE* bands lagging the ATLAS bands spanned +150–240 d, but with uncertainties of 250–330 d, so we cannot comment on any dust reprocessing activity.

[7] The XMM-ULS provided the 0.2–2 keV flux for this observation; we used the best-fitting model to XM3 (Sect. 4.1) to infer its 0.5–2 keV flux.

4. X-ray spectral fits

Our spectral fitting strategy was to start by modeling the *XMM-Newton* EPIC spectra as they had the highest S/N. We then modeled the lower S/N eRASS and *Swift* XRT spectra.

All the X-ray spectral fits were done using XSPEC (Arnaud 1996) version 12.13.0c. All parameter uncertainties are for one interesting parameter, and were derived via Monte Carlo Markov chains (MCMC) using the CHAIN routine in XSPEC. We used the Goodman-Weare MCMC sampler (Goodman & Weare 2010), chains of length 10000, 20 walkers, and a burn length of 5000. Parameter errors are at the 90% confidence level, and are taken from the 5th and 95th percentile values of the parameter distribution. In all models, we included a TBABS component to account for Galactic absorption by H I and H_2 totaling 7.37×10^{20} cm^{-2} (Willingale et al. 2013). We assumed the abundances of Wilms et al. (2000).

4.1. XMM-Newton EPIC spectral fits

For each observation, we fit pn0 (pattern 0; 0.25–10 keV) + pn14 (patterns 1–4; 0.5–10 keV) + MOS1 + MOS2 (both 0.2–10 keV) jointly. We applied instrumental constant components for cross-calibration purposes, keeping the constant for pn0 fixed at unity; constants for the other spectra were usually within a few percent of unity for the best-fitting models. All spectra were grouped to 20 counts per bin to ensure the use of χ^2 statistics.

For all three observations, we found excellent fits consisting of the following baseline model, which is very typical for nearby, X-ray-unobscured Seyferts:

- A hard X-ray power law (ZPOWERLW) to model emission from the hot, optically thin corona.
- A soft X-ray excess, which we modeled as warm Comptonization of optical/UV thermal photons, following Mehdipour et al. (2011), Porquet et al. (2018), and Petrucci et al. (2018), among others. We used COMPTT (Titarchuk 1994), assumed the sphere geometry, and fixed the seed photon temperature $T_{\rm seed}$ to 20 eV.
- A narrow Fe Kα line is detected in XM1 only: a simple preliminary fit consisting of a narrow (width σ fixed to 10 eV) Gaussian component plus a power-law fit to 2–10 keV yields a line intensity $I_{\rm Fe} = (8.7 \pm 5.6) \times 10^{-7}$ ph cm^{-2} s^{-1} keV^{-1} and equivalent width relative to a hard power law $EW = 220 \pm 142$ eV; a set of 500 Monte Carlo simulations using SIMFTEST indicates that the line is detected at the 99.4% confidence level.
  In our final model, we therefore modeled a narrow Fe Kα line as well as a Compton reflection hump, produced by reflection from distant, neutral material lying out of the line of sight. Specifically, we used UXCLUMPY (Buchner et al. 2019), which assumes a clumpy medium. Given the lack of >10 keV data, we left the following parameters frozen to arbitrary values: the cloud angular Gaussian distribution $\sigma_{\rm TOR}$ set to 30°, cloud column density $N_{\rm H}$ set to 1.0×10^{24} cm^{-2}, and Compton-thick inner ring covering fraction to 0. In addition, we froze the system inclination at 15°, based on the results from fitting a diskline component to the broad Balmer profiles (see Sect. 6).
  For XM2–3, the narrow Fe Kα line was not significantly detected, with $I_{\rm Fe} < 3.4\ (1.5) \times 10^{-6}$ ph cm^{-2} s^{-1} and $EW < 178$ (80) eV in XM2 (XM3). In our final model, we thus included an UXCLUMPY component, but with its normalization frozen at the best-fitting value from XM1, under the assumption that

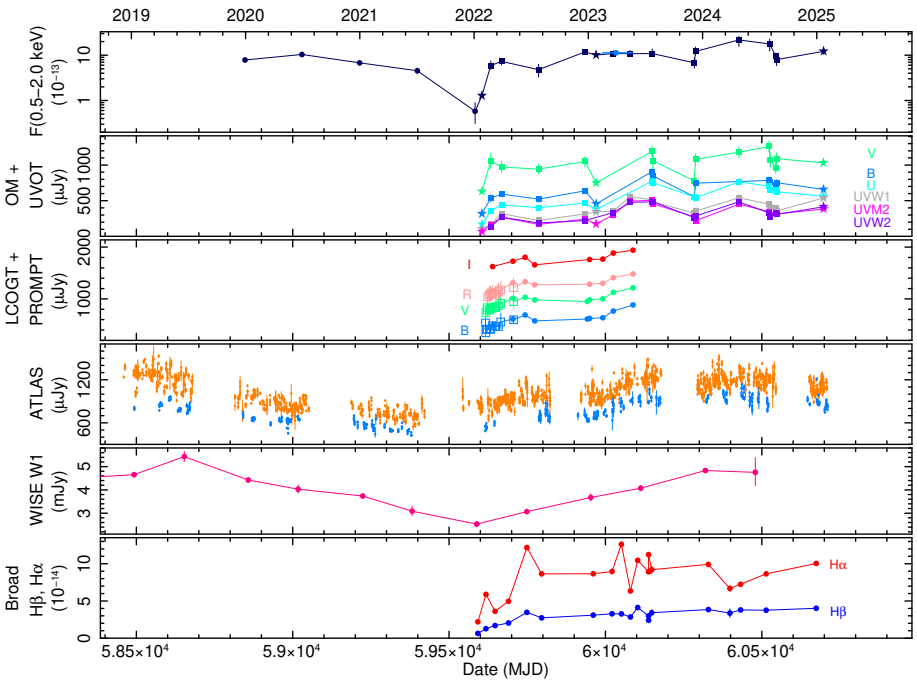

Fig. 1. Multiband continuum and broad Balmer line flux light curves. In the top panel, the black circles, stars, and squares denote X-ray fluxes from eRASS, *XMM-Newton*, and *Swift*, respectively; the blue point denotes the summed NICER data. In the second panel, the stars and squares denotes optical/UV flux densities from *XMM-Newton* and *Swift*, respectively. The third and fourth panels show ground-based optical photometry from LCO+PROMPT and ATLAS, respectively; orange and cyan respectively denote the ATLAS *o* and *c* bands. The fifth panel shows the *NEOWISE* W1 band photometry. For the UV, optical, and IR fluxes plotted here, no host galaxy subtraction has been done; differences in apertures and seeing among the various datasets have resulted in different levels of host contribution. The last panel shows the broad Balmer line fluxes (see §6). Across all panels, all data are plotted with error bars, but some error bars are smaller than the data symbols.

the hard X-ray power-law component has varied between XM1 and XM2, but the distant material has not responded on timescales of 1–3 years.

We obtained excellent fits to all three observations, with the best-fitting parameters listed in Table 1. The spectral data, best-fitting models, and data–model residuals are plotted in Fig. 2. From XM1 to XM2, the hard X-ray power law and the soft X-ray excess increase in flux by factors of $5.5^{+1.1}_{-0.7}$ and $14.1^{+10.3}_{-5.4}$, respectively. Then, from XM2 to XM3, the soft X-ray excess increases by an additional factor of 1.3 ± 0.2, while the hard X-ray power-law flux values are consistent with each other. Values for other spectral parameters, namely T_e and τ in CompTT and Γ_{HX}, are consistent across the three observations.

As an alternate parameterization of the soft X-ray excess, we tested the reflection off an ionized relativistic accretion disk. We removed the CompTT component and replaced it with relxill (García et al. 2014; Dauser et al. 2014), using version v.1.4.3, keeping the outer radius fixed at 400 R_g, and the power-law cut-off energy fixed at 100 keV (though the fit was insensitive to thawing these parameters). We kept the inner radius, black hole spin parameter, disk inclination, disk ionization parameter, Fe abundance relative to the solar value, and power-law emissivity index all free. We also included a narrow Gaussian component (width σ fixed to 10 eV; energy fixed to 6.4 keV) to model any narrow Fe Kα line emission. However, the best-fitting models have values of χ^2/dof that are worse by 20.8, 30.0, and 473.5 for five more degrees of freedom (dof) for XM1, 2, and 3, respectively, compared to the best-fitting models using CompTT,[8] and with worse broadband data/model residuals. We thus did not consider this model further.

We also tested for the presence of line-of-sight obscuration. We tested full-covering neutral obscuration modeled with zTBabs, partial-covering, neutral obscuration modeled with TBpcf, and ionized obscuration modeled with zxipcf, with values of log(ξ, erg cm s^{-1}) set to +1. For all three *XMM-Newton* observations, we found no improvement to our model in either observation when adding various absorption components; AIC increases, and upper limits on N_H were always less than a few times 10^{21} cm^{-2}.

4.2. Spectral modeling of eRASS, Swift XRT, and NICER

For the *Swift* XRT spectra, the number of 0.2–10 keV spectral counts was always small, less than 330 in all cases. We combined Sw7 – Sw8 and Sw12 – Sw13, as those pairs of observations were separated by only three and four days, respectively.

For eRASS and XRT data, we binned each spectrum to 15 counts per bin when the number of spectral counts was above 100 (eR1, eR2, eR3, Sw1, Sw2, Sw6, Sw7-8, Sw10, and Sw14) or to 10 counts per bin when the number of counts was less than 100 (eR4, Sw3, Sw5, Sw9, Sw11, Sw12-13, Sw15). We fit using the C-statistic. In all cases, a single power law modified by the Galactic column provided an excellent fit. The photon index in eR5 was unconstrained, so we froze it to 2.0, the value obtained from fitting a single power law to the 0.5–2.0 keV XM1 spectrum. The best-fitting photon indices and fluxes are listed in Table 2. Photon indices are usually poorly constrained, and there is no evidence of spectral variability.

For the NICER data, we added all 28 observations to maximize the S/N. We fit the 0.4–4.0 keV spectrum. A simple power law yielded a poor fit, so we applied the best-fitting model from XM2 (CompTT + hard power law + UxClumpy). T_e and τ were highly degenerate, so we froze τ at 11, the best-fitting value from XM2; similarly, we froze Γ_{HX} at 1.66. Our best-fitting model has χ^2/dof=47.22/30, $T_e = 0.23^{+0.02}_{-0.01}$ keV, $F_{\rm CompTT,0.2-0.7} = 2.61^{+0.29}_{-0.27} \times 10^{-12}$ erg cm^{-2} s^{-1}, a 0.4–4.0 keV Galactic absorption-corrected power-law flux of $(1.52 \pm 0.03) \times 10^{-12}$ erg cm^{-2} s^{-1}, and an observed absorbed 0.5–2.0 keV flux of $(1.32 \pm 0.01) \times 10^{-12}$ erg cm^{-2} s^{-1}.

[8] Furthermore, the Akaike information criterion (AIC; Akaike 1973) with finite sample correction by Sugiura (1978) yields that ΔAIC going from CompTT to relxill is always positive (+29.3, +38.3, and +481.6, respectively.)

Table 1. Best-fitting models to *XMM-Newton* EPIC spectra

Component/ Parameter	XM1 (MJD 59604.9)	XM2 (MJD 59970.2)	XM3 (MJD 60697.4)
	Hard X-ray power law		
$\Gamma_{\rm HX}$	$1.64^{+0.17}_{-0.09}$	$1.65^{+0.16}_{-0.13}$	$1.83^{+0.09}_{-0.13}$
$F^{(a)}_{\rm PL,2-10}$ (erg cm^{-2} s^{-1})	$2.53^{+0.18}_{-0.33} \times 10^{-13}$	$1.40^{+0.06}_{-0.09} \times 10^{-12}$	$1.38^{+0.03}_{-0.07} \times 10^{-12}$
	CompTT		
$T_{\rm seed}$ (eV)	20*	20*	20*
$T_{\rm e}$ (keV)	$0.29^{+0.29}_{-0.15}$	$0.52^{+0.40}_{-0.18}$	$0.54^{+0.36}_{-0.12}$
τ	12^{+9}_{-5}	9 ± 3	8 ± 2
$F^{(b)}_{\rm CompTT,0.2-0.7}$ (erg cm^{-2} s^{-1})	$8.6^{+2.9}_{-3.2} \times 10^{-14}$	$1.21^{+0.15}_{-0.21} \times 10^{-12}$	$1.59^{+0.21}_{-0.16} \times 10^{-12}$
	UxClumpy		
Inclination, i	15°*	15°*	15°*
$\sigma^{(c)}_{\rm tor}$	30°*	30°*	30°*
CTK Cov. Frac.$^{(d)}$	0*	0*	0*
log($N_{\rm H}$, cm^{-2})	24.0*	24.0*	24.0*
Normalization (ph keV^{-1} cm^{-2} s^{-1})	$6.3^{+4.5}_{-2.5} \times 10^{-4}$	6.3×10^{-4}*	6.3×10^{-4}*
Observed F_{2-10} (erg cm^{-2} s^{-1})	$2.93^{+0.17}_{-0.20} \times 10^{-13}$	$1.47^{+0.06}_{-0.07} \times 10^{-12}$	$(1.44 \pm 0.04) \times 10^{-12}$
Observed $F_{0.5-2.0}$ (erg cm^{-2} s^{-1})	$(1.28 \pm 0.04) \times 10^{-13}$	$1.01^{+0.02}_{-0.03} \times 10^{-12}$	$1.22^{+0.01}_{-0.08} \times 10^{-12}$
$L^{(e)}_{2-10}$ (erg s^{-1})	$6.0^{+0.4}_{-0.8} \times 10^{42}$	$3.2^{+0.1}_{-0.2} \times 10^{43}$	$3.3^{+0.1}_{-0.2} \times 10^{43}$
χ^2/dof	358.69/341	531.14/584	1395.70/1445

Notes. An asterisk (*) denotes a fixed parameter.
(a) 2–10 keV flux of the hard power-law component, corrected for Galactic absorption
(b) 0.2–0.7 keV flux of the CompTT component, corrected for Galactic absorption
(c) Denotes the cloud angular Gaussian distribution in UxClumpy
(d) Denotes that we fixed the covering fraction of the Compton-thick inner ring in UxClumpy to 0
(e) Denotes the 2–10 keV luminosity corresponding to the hard X-ray power-law component.

Table 2. Best-fitting power-law models to eRASS and *Swift* XRT spectra.

Obs. (Date)	C-stat/dof	Power-Law Photon Index	Observed $F_{0.5-2.0}$ (10^{-13} erg cm^{-2} s^{-1})$^{(a)}$
eR1 (MJD 58847.5)	12.93/10	2.31 ± 0.29	$9.16^{+1.24}_{-0.96}$
eR2 (MJD 59029.6)	12.65/10	2.43 ± 0.32	$9.32^{+1.01}_{-1.26}$
eR3 (MJD 59213.9)	0.73/4	2.04 ± 0.51	$6.92^{+1.21}_{-1.21}$
eR4 (MJD 59398.3)	6.09/4	2.30 ± 0.57	$3.08^{+0.99}_{-0.92}$
eR5 (MJD 59583.3)	2.97/2	2.0*	$0.58^{+0.32}_{-0.27}$
Sw1 (MJD 59633.3)	0.75/3	1.95 ± 0.46	$5.9^{+1.3}_{-1.1}$
Sw2 (MJD 59667.7)	3.35/6	2.12 ± 0.30	7.3 ± 1.2
Sw3 (MJD 59786.3)	2.55/2	1.83 ± 0.79	4.8 ± 1.5
Sw4 (MJD 59934.3)	15.87/18	2.25 ± 0.17	$11.8^{+1.3}_{-1.1}$
Sw5 (MJD 60025.5)	2.71/4	2.66 ± 0.48	$7.2^{+1.5}_{-1.6}$
Sw6 (MJD 60078.6)	8.54/7	2.33 ± 0.30	10.9 ± 1.6
Sw7–8 (MJD 60148–51)	4.65/10	$2.51^{+0.33}_{-0.30}$	$10.9^{+2.8}_{-1.5}$
Sw9 (MJD 60284.3)	3.19/3	1.77 ± 0.54	$6.8^{+1.9}_{-1.6}$
Sw10 (MJD 60288.1)	1.87/3	2.04 ± 0.52	$12.1^{+3.1}_{-2.1}$
Sw11 (MJD 60426.7)	2.39/3	$2.48^{+0.50}_{-0.48}$	$21.8^{+4.6}_{-6.3}$
Sw12–13 (MJD 60523–7)	3.70/4	$2.39^{+0.78}_{-0.67}$	$17.7^{+5.1}_{-5.2}$
Sw14 (MJD 60544.7)	1.54/5	1.85 ± 0.32	$9.5^{+1.6}_{-1.5}$
Sw15 (MJD 60547.1)	9.01/2	$2.48^{+0.60}_{-0.57}$	$8.0^{+2.3}_{-2.1}$

Notes. An asterisk (*) denotes a fixed parameter; specfically, the photon index in eR5 was completely unconstrained.
(a) Observed (Galactic-absorbed) 0.5–2.0 keV flux.

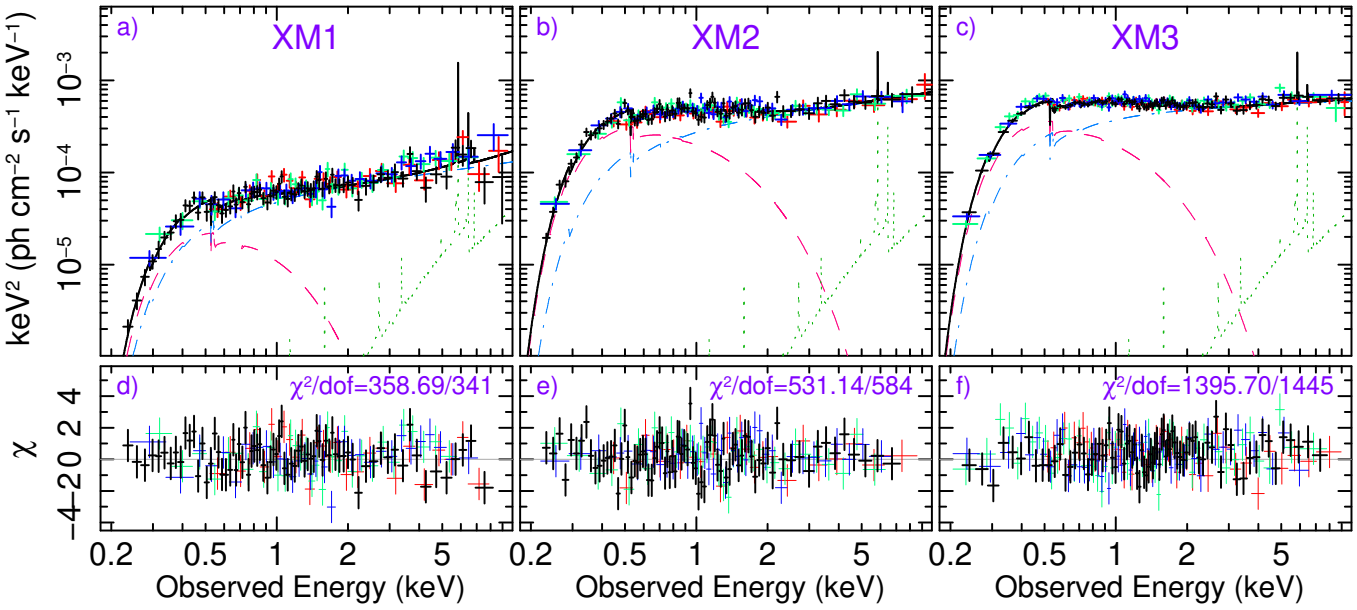

Fig. 2. Spectral data and fits for XM1–3. Black, red, green, and blue denote pn0, pn14, MOS1, and MOS2, respectively. The data have been rebinned by factors of 2, 3, and 6 in XM1, XM2, and XM3, respectively, for clarity. Panels a–c display the best-fitting unfolded models and data. The CompTT, hard X-ray power-law, and UxClumpy components are respectively denoted by red dashed, blue dash-dotted, and green dotted lines, and the total model is denoted by a black solid line. The corresponding χ residuals are plotted in panels d–f.

5. Broadband SED modeling

We constructed optical/UV/X-ray SEDs at several selected points in time to track the broadband spectral evolution as the source luminosity recovered. We fit XM1, Sw1, Sw3, Sw4, XM2, Sw7, Sw11, and XM3, using either OM+EPIC pn or XRT+UVOT. For Sw1, Sw3, Sw4, and XM2, we augmented these SEDs with data points constructed from quasi-simultaneous (to within 21 days) BVRI photometry obtained from the LCOGT observations that were closest in time; the datasets used are listed in Table 3. We did not correct the optical and UV data points for Galactic reddening prior to fitting. We included a 5% systematic uncertainty to account for differences in filter responses, as well as for the fact that most LCOGT and X-ray/UV observations were not strictly simultaneous, and some mild variability intrinsic to the AGN may have occurred.

The resulting SEDs are plotted in Fig. 3; the spectral variability, particularly in the optical/UV regime, is readily apparent. We fit a model consisting of fAGNSED (Kubota & Done 2018; Hagen & Done 2023) plus an Sb host galaxy template from the SWIRE template library (Polletta et al. 2007) to account for host galaxy starlight, with both components absorbed and reddened only by our Galaxy. For Galactic reddening, we set $E(B-V)$ to 0.057, based on the dust maps of Schlegel et al. (1998). fAGNSED posits three emission regions: an optically thick, geometrically thin outer disk that encircles a warm Comptonizing region, which in turn encircles a geometrically thick, optically thin, hot Comptonizing region. In all fits we froze the co-moving distance to the source at 404 Mpc, the normalization at unity, the black hole mass to 1.4×10^8 $M_\odot$, derived via the width of the broad Hβ emission lines as discussed in Sect. 6.3, the dimensionless black hole spin parameter $a*$ at zero, the electron temperature of the hot corona, $k_B T_{e,hot}$, at 100 keV, the hot corona's scale height at 10 R_g, and the inclination angle of the warm corona and outer disk at 15°. In addition, we kept the radial size of the warm corona, R_{warm}, fixed to twice that of the hot corona, R_{hot}, in all fits. The outer radius of the disk was calculated via the self-gravity radius from Laor & Netzer (1989), and reprocessing was included. Compared to AGNSED, fAGNSED includes a color–temperature correction for the accretion disk emission, f_{col}, which we left as a free parameter. For the XM1–3 fits, which had the best signal-to-noise ratio, the free parameters were the accretion rate relative to Eddington, $\dot{m}_{Edd}$, the electron temperature of the warm corona, $k_B T_{e,warm}$, the spectral indices of the warm (Γ_{warm}) and hot (Γ_{hot}) Comptonization components, the outer radius of the hot Comptonizing component, R_{hot}, and the normalization of the host galaxy template. For the fits using *Swift* data, to obtain reasonable constraints on free parameters, we froze R_{hot} to 26 R_g and $k_B T_{e,warm}$ to 0.16 keV, the averages of the best-fitting values from XM1–3. For all fits except Sw4+LCO6, Γ_{warm} was very poorly constrained, so we froze it to 2.3. Sw4 had the highest S/N soft X-ray data of all XRT observations, and thawing Γ_{warm} yielded a fit that was an improvement at the 99.8% confidence level compared to leaving Γ_{warm} frozen at 2.3 according to an F-test. Finally, we included a torus component modeled with UxClumpy, with all parameters frozen to values used in the *XMM-Newton*-only fits (Table 1).

The best-fitting model parameters are listed in Table 3. For brevity, the best-fitting values of the normalization of the host galaxy template are omitted from that table; the best-fitting values are always in the range (8–11)$\times 10^{-16}$ erg cm^{-2} s^{-1} Å^{-1}. The best-fitting values of $\dot{m}_{Edd}$ increase steadily over 3 years, by a factor of 7 from XM1 to XM3. We list the estimates of the unabsorbed bolometric luminosity, L_{Bol}, at all epochs; L_{Bol} is as low as 6.4×10^{43} erg s^{-1} during XM1. We also list the 13.6 eV – 10 keV ionizing luminosity, L_{ion}, calculated from integrating over the best-fitting unabsorbed models, and useful for discussion in Sect. 7 regarding Balmer line emission; they also increase by a factor of roughly 7 from XM1 to XM3. The values of L_{Bol}/L_{2-10} for XM1, 2, and 3 are thus 11, 8, and 13, respectively, consistent with expectations for Seyfert AGN at this luminosity (Duras et al. 2020). The best-fitting values of Γ_{hot} and $k_B T_{e,warm}$ are consistent across XM1–3, precluding any evidence for evolution in those parameters. In particular, photon counts above 3 keV are poor for Sw1, Sw3, Sw4, and Sw7, so those values

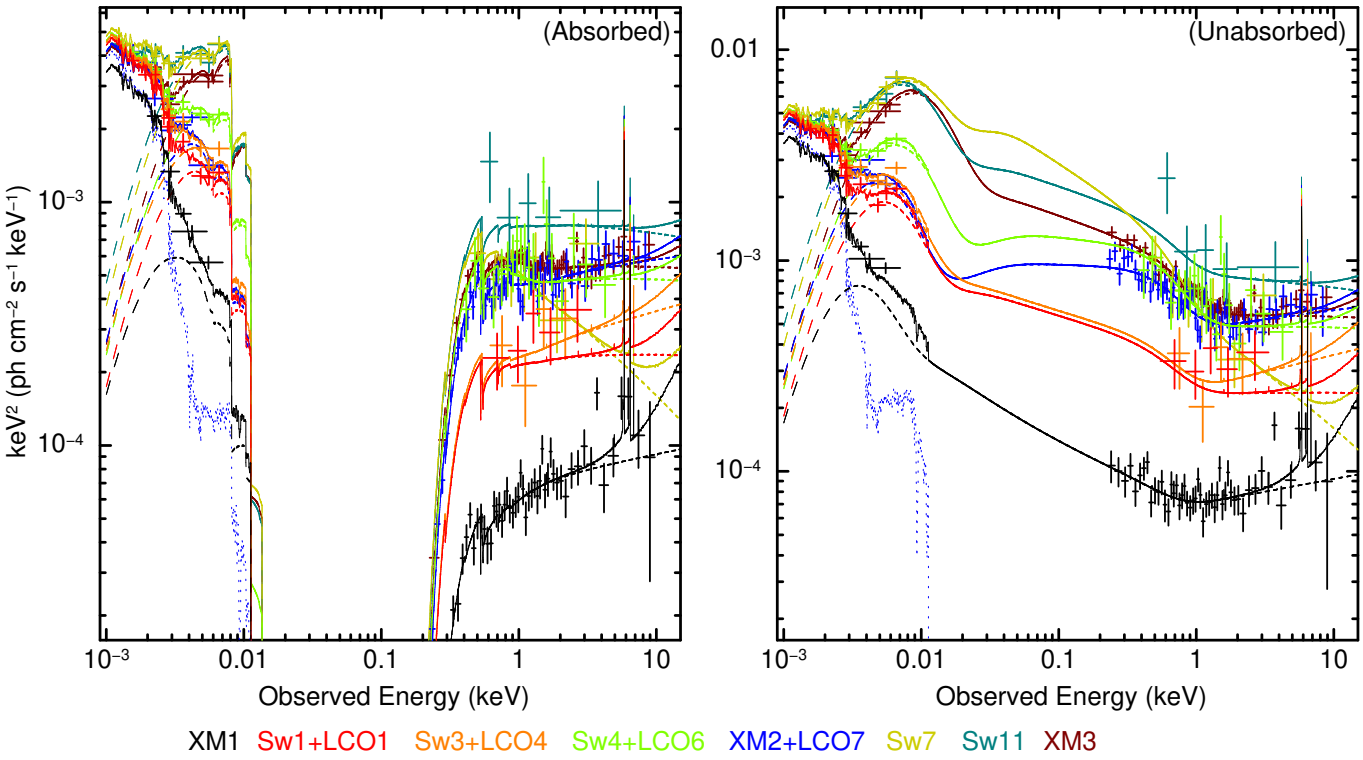

Fig. 3. Optical/UV/X-ray SEDs and best-fitting models. In the left panel the data points are not corrected for Galactic reddening or obscuration, and best-fitting models are reddened or obscured. In the right panel, both data and models are unreddened and unobscured. The dashed lines represent the best-fitting fAGNSED components. The dotted line indicates the host galaxy template (for clarity, only displayed for the XM2 fit). The solid lines represent the total model; a torus component is included in the modeling but for clarity is displayed here only as part of the total model. For the *XMM-Newton* fits, only the EPIC pn0 data were used. XM1, XM2, and XM3 pn0 data were rebinned by factors of 3, 4, and 7 for plotting purposes only.

of $\Gamma_{\rm hot}$ may be subject to artefacts of modeling and should be interpreted with caution. The best-fitting absorbed and unabsorbed models are plotted in Fig. 3.

6. Fits to optical emission-line spectra

The 21 rest-frame optical spectra are plotted in Fig. 4, with a zoom-in on the Hβ region for selected spectra in Fig. 5. Visually, the broad Balmer profiles are very weak during the low-continuum state in January–February 2022 (#3–#4). During March–August 2022 (#5–#8), as optical, UV, and X-ray continuum fluxes rise, the broad Balmer profiles become stronger, but remain roughly Gaussian-like (Fig. 5, left panel). However, by January 2023 (spectrum #9), the broad Balmer profiles become much more boxy in shape.

Other features in the spectra include Fe II emission near 4570 Å, and narrow lines due to [O III], [N II], [S II], [Ne V], and the Balmer series. There is also some broad He I λ5876 emission, prominent in the H/ESO spectrum (#2), then very weak during spectra #3–4, then with strength gradually increasing throughout the rest of the campaign.

6.1. Summary of spectral fit procedure

Spectral modeling was done with the Python LMFIT package (Newville et al. 2014). We masked a region of atmospheric telluric absorption, 6843–6900 Å (observed frame, corresponding to 6242–6293 Å rest frame). A second region of telluric absorption impacted a narrow region near 7175 Å observed frame (6544 Å rest frame), in the broad Hα profile and very close to [N II] λ6548. We modeled the Hβ (4200-5400 Å rest frame) and Hα regions (5600–6900 Å rest frame) separately. For the AGN continuum, we used a broken power-law model. We used an Sb host galaxy template from the SWIRE library (Polletta et al. 2007). We used the Fe II templates of Kovačević et al. (2010) for Hβ range since it can model the F, S, G, P, and I Zw 1 groups of Fe II separately, though in our fits, the P and Z group amplitudes fell to zero. We used the Bruhweiler & Verner (2008) template for the Hα fits, given the limited wavelength coverage of the Kovačević et al. (2010) templates. The Fe II velocity widths are typically of order 2500 km s^{-1}.

Our fits to the Hβ region contained Gaussians for narrow-line emission from Hβ, [O III] $\lambda\lambda$5007,4959, and [O III] λ4363, with all velocity widths σ tied to that of [O III] λ5007 (typically 150–350 km s^{-1}). The [O III] $\lambda\lambda$5007,4959 profiles each required an additional broad but weak blueshifted Gaussian component, with velocity width typically 250–800 km s^{-1} and velocity offset typically 150–400 km s^{-1}. Such features are indicative of a NLR outflow in J1240–2309, similar to those inferred for many nearby as well as high-redshift AGN (Schmidt et al. 2018; Leung et al. 2019).

In the Hα region, we included narrow Gaussians for [N II] $\lambda\lambda$6583,6548, [S II] $\lambda\lambda$6731,6716, and [O I] λ6300, with these lines' velocity widths tied. We also included a broad Gaussian to model He I λ5876 emission; for all spectra except #3–4, and #8 (low S/N), it was detected and modeled well with a Gaussian of width σ typically 35–55 Å, with no evidence of evolution in σ. To model the narrow atmospheric telluric feature at 7175 Å observed frame (6544 Å rest frame), we obtained a good fit us-

Table 3. Best-fitting broadband SED models using fAGNSED.

Dataset and date (MJD)	$\log(\dot{m}_{\rm Edd})$	$f_{\rm col}$	$k_{\rm B}T_{\rm e,warm}$ (keV)	$\Gamma_{\rm warm}$	$\Gamma_{\rm hot}$	$R_{\rm hot}$	$L_{\rm ion}{}^{(a)}$ (erg s^{-1})	$L_{\rm bol}{}^{(b)}$
XM1 (59604)	$-2.44^{+0.01}_{-0.08}$	$1.08^{+0.57}_{-0.04}$	$0.14^{+0.74}_{-0.04}$	2.54 ± 0.10	$1.88^{+0.17}_{-0.16}$	$22.6^{+7.7}_{-0.4}$	3.2×10^{43}	6.4×10^{43}
χ^2/dof = 145.36/150								
Sw1 (59633)	$-2.03^{+0.04}_{-0.02}$	$1.53^{+0.34}_{-0.27}$	0.16*	2.3*	$2.00^{+0.15}_{-0.13}$	26*	1.1×10^{44}	1.6×10^{44}
+ LCO1 (59639)								
χ^2/dof = 15.52/11								
Sw3 (59786)	-1.94 ± 0.03	$1.42^{+0.31}_{-0.20}$	0.16*	2.3*	$1.84^{+0.31}_{-0.17}$	26*	1.2×10^{44}	2.0×10^{44}
+ LCO4 (59773)								
χ^2/dof = 12.58/10								
Sw4 (59934)	$-1.75^{+0.03}_{-0.02}$	$1.69^{+0.31}_{-0.17}$	0.16*	$2.09^{+0.12}_{-0.07}$	$2.01^{+0.11}_{-0.12}$	26*	2.4×10^{44}	3.1×10^{44}
+ LCO6 (59949)								
χ^2/dof = 21.62/25								
XM2 (59970)	$-1.81^{+0.02}_{-0.01}$	$1.50^{+0.26}_{-0.23}$	$0.16^{+0.04}_{-0.03}$	$2.08^{+0.08}_{-0.05}$	$1.91^{+0.11}_{-0.10}$	$31.8^{+2.1}_{-1.2}$	1.9×10^{44}	2.7×10^{44}
+ LCO7 (59991)								
χ^2/dof = 261.06/248								
Sw7 (60148)	$-1.50^{+0.05}_{-0.02}$	$1.67^{+0.43}_{-0.24}$	0.16*	2.3*	$2.49^{+0.13}_{-0.10}$	26*	4.9×10^{44}	5.5×10^{44}
χ^2/dof= 9.97/9								
Sw11 (60426)	$-1.49^{+0.10}_{-0.03}$	$1.57^{+0.85}_{-0.28}$	0.16*	2.3*	$2.06^{+0.21}_{-0.19}$	26*	4.4×10^{44}	6.1×10^{44}
χ^2/dof= 5.83/6								
XM3 (60697)	$-1.60^{+0.06}_{-0.02}$	$1.86^{+0.38}_{-0.23}$	$0.18^{+0.03}_{-0.02}$	$2.30^{+0.10}_{-0.04}$	$2.00^{+0.06}_{-0.05}$	$21.6^{+1.7}_{-2.7}$	3.6×10^{44}	4.4×10^{44}
χ^2/dof = 442.50/473								

Notes. An asterisk (*) denotes a fixed parameter..
[(a)] 13.6 eV – 10 keV unabsorbed model luminosity.
[(b)] Bolometric unabsorbed model luminosity.

ing a narrow Pearson7 component, though this component was required only for spectra #3, 5, 6, 9, 12–19, and 21.

For each of the broad Hβ and Hα Balmer profiles, a simple broad Gaussian slightly redshifted relative to rest frame and width σ usually 30–50 Å, yields decent fits for the spectra taken in 2022 (#3–#8), but yields poor fits to all later spectra. The later spectra are fit well phenomenologically by the sum of a broad Gaussian plus two additional Gaussians, with equal widths σ and amplitudes on either side of the main broad peak. These two additional Gaussians typically peak at 4845–4852 and 4883–4888 Å (Hβ) and 6535–6548 and 6583–6601 Å (Hα). Consequently, we pursued a more physical modeling using the sum of a broad Gaussian plus a relativistic diskline component (Chen et al. 1989) to model emission across a range of radii in an assumed flat annular region. We fixed the diskline's outer radius $R_{\rm out}$ to 5000 $R_{\rm g}$ in all fits, but left inner radius $R_{\rm in}$ free. We incorporated a local broadening factor, σ_0, to account for electron scattering in a photoionized atmosphere. Some parameters, when left thawed, were not constrained in some fits. In those cases, we froze $R_{\rm in}$ to 1000 $R_{\rm g}$, σ_0 to 10 Å (600 km s^{-1}) for Hβ or to 15 Å (700 km s^{-1}) for Hα, and inclination angle i[9] to 13°, the average of the best-fitting values for the remaining fits. We applied this component to all Hβ and Hα profiles. For all Hα fits, the use of the diskline plus broad Gaussian model is a better fit compared to either a single broad Gaussian or a single diskline component (lower values of AIC and χ^2 in each case) for all spectra. For the Hβ fits, this statement holds true for all spectra except #4, #8, and #11, but we also adopt the diskline plus broad Gaussian model for these fits, on physical grounds. We note that diskline parameters are relatively insensitive to the assumed value of $R_{\rm out}$. For instance, assuming a fiducial value of $R_{\rm out}$=20000 $R_{\rm g}$, i increases by an average of only 3–4°, and $R_{\rm in}$ increases by an average of only 15%.[10] Sample model fits are shown in Fig. 7. Best-fitting values using the diskline plus broad Gaussian model are listed in Tables B.7, B.8, and B.9. The total broad Hβ line flux is plotted as function of time in Fig. 1; the line fluxes increase during 2022–2024, qualitatively tracking the increase in continuum fluxes. We do not find evidence of evolution in the Balmer decrement of the broad Gaussian component, diskline component, or total broad-line fluxes (average values of 2.28, 2.76, and 2.73, respectively).

For the diskline component in the Hβ and Hα fits, the best-fitting values of inclination angle θ (defined such that 0° corresponds to a face-on orientation) are usually 10–15°. The median value and standard deviation of $R_{\rm in}$ across all fits where $R_{\rm in}$ was a free parameter is 1040±410 $R_{\rm g}$. We find no evidence of evolution in either $R_{\rm in}$ or θ parameter with time. For the broad Gaussian components, energy centroids $E_{\rm cent}$ are redshifted by average values of 12±10 Å (770±620 km s^{-1}) for Hβ and 13±8 Å (620±370 km s^{-1}) for Hα. Rest-frame velocity widths σ are typically 1850–3300 km s^{-1} for Hβ and typically 1800–3900 km s^{-1} for Hα, with no evidence of time evolution of these parameters.

We define $F_{\rm DL}$ as the flux of the diskline component relative to the total (broad Gaussian plus diskline) flux. In Fig. 8, we plot values of $F_{\rm DL}$ for both Hβ and Hα as a function of U, UVW1, and

[9] i is defined such that 0° indicates a face-on disk.

[10] Additionally, for this value of $R_{\rm out}$, the values of the parameter $F_{\rm DL}$, discussed below, increase by an average of only 5 percent, and the associated Pearson correlations are not significantly impacted.

UVW2 flux densities, using values interpolated from the combined UVOT plus OM light curves. For both Hβ and Hα there are moderate positive correlations between $F_{\rm DL}$ and UV flux densities. For Hβ, Pearson correlation coefficients (null hypothesis probabilities) for U, UVW1, and UVW2 are 0.614 (0.0052), 0.611 (0.0055), and 0.627 (0.0041), respectively. For Hα, these values are 0.601 (0.0065), 0.700 (0.0008), and 0.628 (0.0040), respectively.

6.2. Subtype evolution

To quantify the evolution in broad Hβ flux, we consider the ratio of the integrated broad Hα flux (sum of diskline and Gaussian; see Table B.7) to the sum of the [O III] λ5007 line (sum of narrow and blueshifted components; see Table B.9), hereafter $\mathcal{R}_{\rm H\beta/[O\,III]}$, as defined in Winkler (1992). We also consider the ratio of broad to narrow Hβ peak flux densities, hereafter $\mathcal{R}_{\rm BL/NL}$, following Runco et al. (2016). The values of $\mathcal{R}_{\rm H\beta/[O\,III]}$ and $\mathcal{R}_{\rm BL/NL}$ are listed in Table B.9, and plotted in Fig. 9. From spectrum #2 (March 2002) to #3 (January 2002), $\mathcal{R}_{\rm H\beta/[O\,III]}$ falls by a factor of 4.3±0.8. $\mathcal{R}_{\rm H\beta/[O\,III]}$ then gradually increases by a factor of almost 6 for the rest of the campaign. The values of $\mathcal{R}_{\rm BL/NL}$ also reach a minimum during spectrum #3 (factors of 5–6 smaller than in #1 and #2), and increase back to their approximate maximum values thereafter.

We can also use $\mathcal{R}_{\rm H\beta/[O\,III]}$ and $\mathcal{R}_{\rm BL/NL}$ and to assign approximate Seyfert subtype classification. Winkler (1992) assigned subtypes 1.0, 1.2, 1.5, and 1.8 to objects with $\mathcal{R}_{\rm H\beta/[O\,III]} > 5$, $2 < \mathcal{R}_{\rm H\beta/[O\,III]} < 5$, $0.33 < \mathcal{R}_{\rm H\beta/[O\,III]} < 2$, and $\mathcal{R}_{\rm H\beta/[O\,III]} < 0.33$, respectively. Meanwhile, Runco et al. (2016) assigned subtypes 1.0, 1.5, and 1.8 to objects with $\mathcal{R}_{\rm BL/NL} > 1.25$, $0.6 < \mathcal{R}_{\rm BL/NL} < 1.25$, and $\mathcal{R}_{\rm BL/NL} < 0.6$, respectively. These classification boundaries, and the evolution with respect to them, are plotted in Fig. 9. For example, under the Runco et al. (2016) scheme, J1240–2309 was type 1.0 in 1993 and 2002 (#1–2), transitioned to type 1.8 by January 2022 (#3), and returned to type 1.0 by April 2022 (#6 onward).

However, we recall some brief caveats regarding the use of these quantities for subtype classification: In general, comparison from one object to the next means comparing objects with potentially different NLR properties and/or host galaxy star formation activity. In addition, the impact of the host galaxy continuum in the spectrum (and how accurately it is modeled) can be strong when the broad Hβ line is weak. Finally, spectra taken with different apertures can yield different measurements of [O III] flux and host galaxy light, for example.

Nonetheless, in summary, we have tracked strong evolution in the J1240–2309 broad Hβ profile — as quantified by large changes in $R_{\rm H\beta/[O\,III]}$ and $R_{\rm BL/NL}$, and evolution across subtype assignments — both from 2002 to the low-continuum state in January 2022, and during 2022–2024 as the continuum rebrightened. This evolution is qualitatively consistent with that observed in multiple other CLAGN, even on timescales as short as months, such as 1ES 1927+654 (Trakhtenbrot et al. 2019), NGC 5548 (Shapovalova et al. 2009), and Mkn 1018 (Lu et al. 2025).

6.3. Estimation of black hole mass

We can obtain an estimate for the black hole mass, $M_{\rm BH}$, using the width of the broad Hβ line and the empirically derived dependence of BLR Hβ weighted emission radius, $R_{\rm BLR}$, on optical (Bentz et al. 2009, 2013) and/or UV (Kilerci Eser et al. 2015) luminosity. To minimize the impact that the dip-then-recovery transient event had on the illumination and ionization structure of the BLR during 2022, we consider the average of widths of the broad Hβ Gaussian component during spectra #12–19, which are likely more representative of J1240–2309 in a persistent, nontransient-event state. The H/ESO and 6dF archival spectrum were not flux calibrated, so we do not consider them here.

We find an average flux density at 5100 Å (rest frame), $F_{5100\text{Å}} = (5.1 \pm 0.3) \times 10^{-16}$ erg cm^{-2} s^{-1} Å^{-1}. For a luminosity distance of 443 Mpc, the monochromatic optical luminosity $\lambda L_{5100\text{Å}} = (6.1 \pm 0.4) \times 10^{43}$ erg s^{-1}. We apply the best-fitting $\lambda L_{5100\text{Å}} - R_{\rm BLR}$ relation of Bentz et al. (2013), $\log(R_{\rm BLR}, \text{lt-dy}) = (1.56 \pm 0.02) + (0.55 \pm 0.03)\log(\lambda L_{5100\text{Å}}/(10^{44}\ \text{erg s}^{-1}))$. We obtain $R_{\rm BLR} = (7.1 \pm 0.8) \times 10^{16}$ cm = 27 ± 3 lt-dy. The average FWHM of the broad Hβ Gaussian was 5930 ± 240 km s^{-1}. Using the best-fitting relation between virial factor f and FWHM from Mejía-Restrepo et al. (2018), we obtain $f = 0.8$. This yields $M_{\rm BH} = f R_{\rm BLR} v^2_{\rm FWHM} G^{-1} = (1.4 \pm 0.6) \times 10^8\ {\rm M}_\odot$, where we have increased the uncertainty by 0.5 dex given the scatter in the relationship between reverberation-mapped masses and single-epoch mass estimation (e.g., Vestergaard & Peterson 2006).

7. Discussion

7.1. Review of main observational results

- Thanks to eROSITA's all-sky X-ray surveys, we detected a dip in the soft X-ray (0.5–2 keV) flux in J1240–2309 by a factor of $17.0^{+16.3}_{-7.2}$ over 18 months, from eRASS2 to eRASS5.
- Our follow-up campaign tracked the subsequent recovery from the continuum dip in the X-ray band, and tracked a concurrent increase in the UV and optical bands. Compared to the lowest fluxes measured, in January 2022 (XM1), the soft X-ray flux rose by a factor of roughly 9 by 2023–2024 (average of all data points from December 2022 – April 2024). Concurrently, the far-UV flux increased by a factor of roughly 5.
- The IR continuum as traced with *WISE* indicates a stable accretion rate through 2019, but also shows a flux dip starting in ∼2020 and a subsequent flux recovery during 2022–2024. The variable component of IR continuum emission in Seyferts typically originates in warm circumnuclear dust that reprocesses disk and coronal photons. The IR variability behavior in J1240–2309 and the lack of a significant neutral X-ray-obscuring gas column along the line of sight both thus strongly favor a scenario where the continuum behavior is intrinsic to the emission disk and corona, as opposed to being caused by the transit of a dusty, compact obscuring cloud across the line of sight to the inner disk and corona.
- A thermal Comptonization model (fAGNSED) can successfully describe all SEDs well. The value of $\dot{m}_{\rm Edd}$ increases by a factor of 7 over 3 years, from 0.0036 to 0.025. There is no strong evidence for evolution in the warm corona temperature nor in the parameters of the hot corona.
- Our optical spectral monitoring program uncovered significant evolution in the broad Balmer fluxes and profiles that tracked the continuum flux variability over timescales of months–years. $\mathcal{R}_{\rm H\beta/[O\,III]}$ ($\mathcal{R}_{\rm BL/NL}$) decreased by a factor of 2–4 (5–6) from 1993 and 2002 to the low-flux state in January 2022. As continuum flux increased during 2022–2024, $\mathcal{R}_{\rm H\beta/[O\,III]}$ ($\mathcal{R}_{\rm BL/NL}$) increased by a factor of roughly 6 (5). Under the Runco et al. (2016) subtype classification, J1240–2309 was subtype 1.0 in the archival spectra, 1.8 in January 2022, and back to 1.0 by mid-2022.

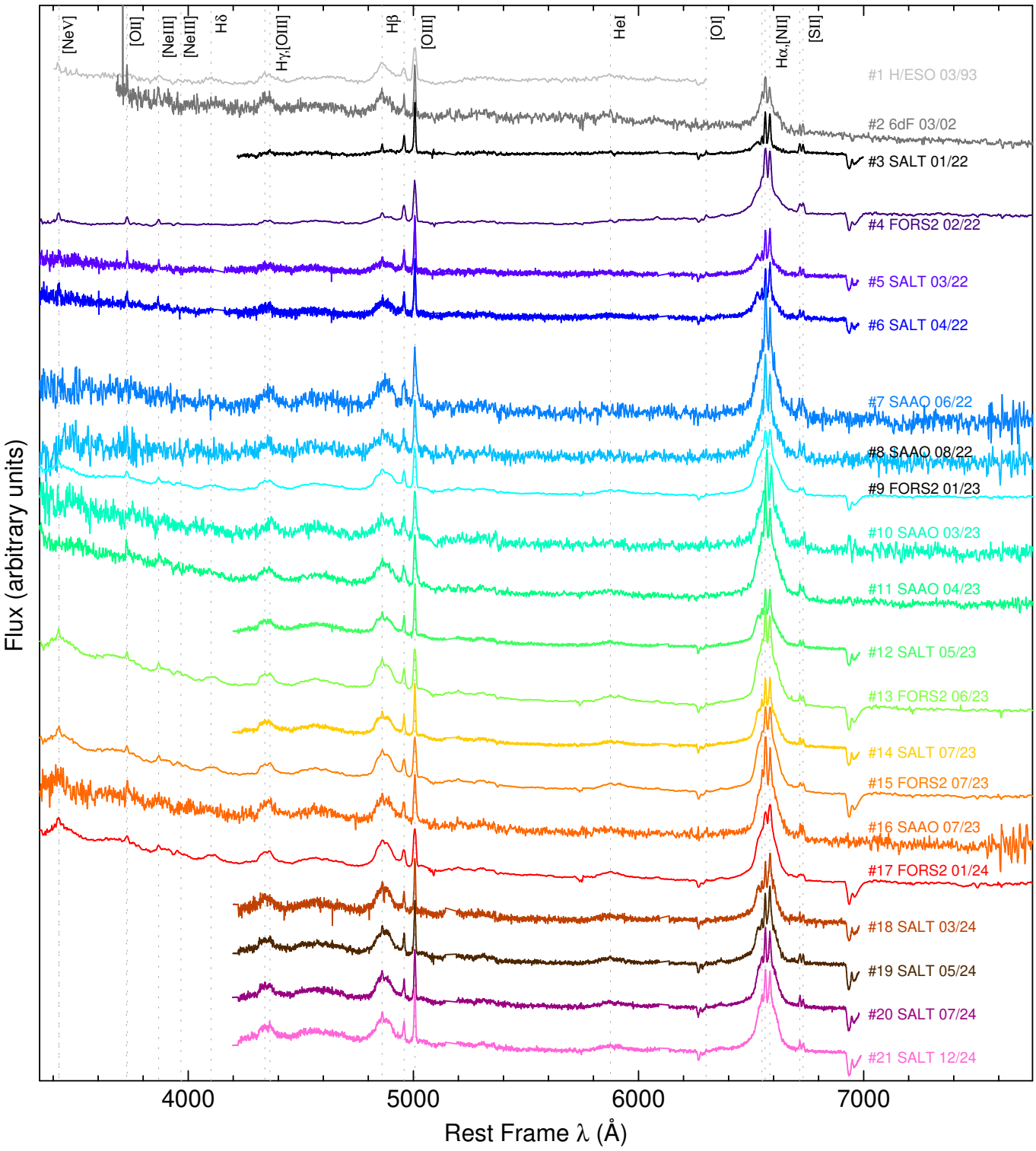

Fig. 4. All 21 optical spectra considered for spectral fitting, plotted with arbitrary shifts for visual clarity.

– The broad Hβ and Hα profiles can each be modeled as the sum of a broad (width σ typically 30–50 Å), slightly redshifted Gaussian plus a double-peaked diskline component. The best-fitting diskline component has an inclination of 10–15°, and an inner radius typically of 600–1500 R_g (with the outer radius assumed fixed at 5000 R_g). The diskline's fractional contribution to the total observed profile, F_{DL}, is low during the continuum dip: 0.1–0.2 during spectra #3–4 for both Hβ and Hα. However, as the overall continuum flux recovers, F_{DL} increases to roughly 0.4 for Hβ and 0.6 for Hα, and we find significant correlations between F_{DL} and UV continuum fluxes for both Hβ and Hα.

7.2. Mechanisms driving evolution in accretion rate

J1240–2309 is yet another CLAGN where a change in accretion rate seems the most likely driver; as mentioned above, a change in obscuration would not cause mid-IR luminosity to dip and

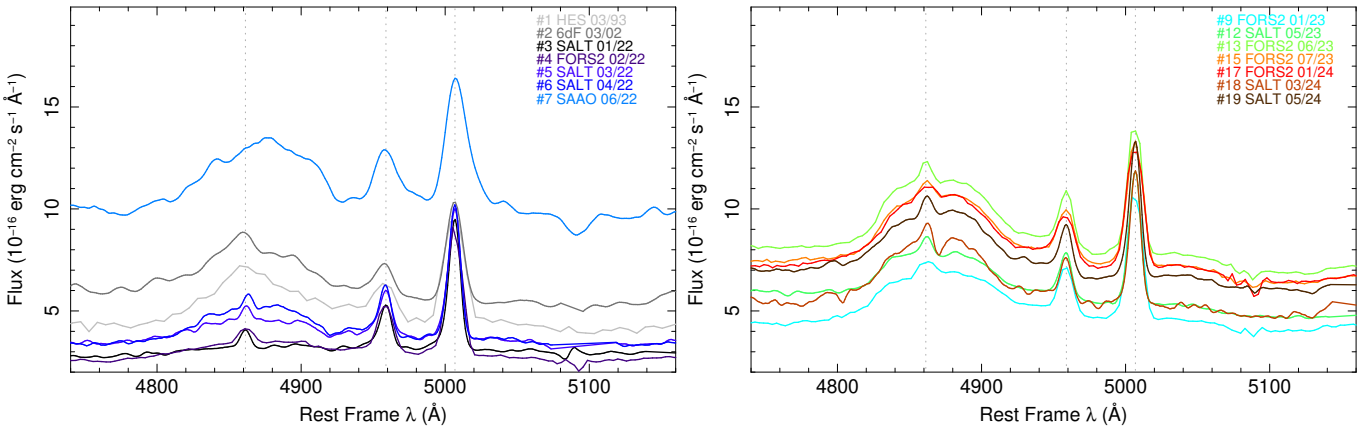

Fig. 5. Hβ and [O III] regions of selected optical spectra. The latter spectra (right panel) correspond to the resurgence of the diskline component, as discussed below. These spectra have been gray-scaled so that the integrated [O III] fluxes match. Smoothing has been applied for visual clarity only, using a boxcar of width 5 Å for all spectra, except for #2 and #7 where the width was 10 Å.

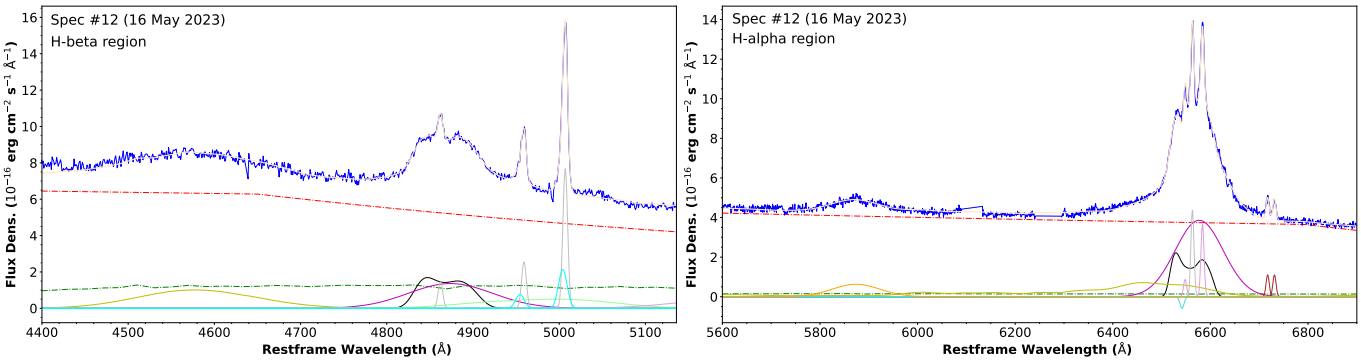

Fig. 6. Sample spectral decomposition in the Hβ (left) and Hα (right) regions for spectrum #12. In each panel, the blue solid line denotes the data, the total model is shown in beige, the solid black line denotes the Balmer diskline component, the solid magenta line denotes the broad Balmer Gaussian component, the red dashed line denotes the power-law component, and the dark green dashed line denotes the host galaxy emission. In the left panel (Hβ), yellow, pale green, and pink respectively denote the F-, S-, and G-groups of Fe II emission, while the narrow Balmer and [O III] components are shown in gray, and the broad blueshifted [O III] components are shown in cyan. In the right panel (Hα), He I emission is shown in orange, [S II] emission is shown in brown, [N II] emission is shown in pink, and the telluric atmospheric absorption feature is shown in cyan.

recover concurrently to the X-ray and optical/UV bands. Using the IR flux as a proxy for optical/UV continuum flux prior to 2022, we can assign a time of 2–3 years for the optical/UV luminosity drop. The time for optical/UV luminosity to increase can also be 2–3 years, but constraints are limited by the length of our campaign. Meanwhile, the X-ray dip and recovery timescales are shorter, but difficult to define given the limited cadence of the eRASS and WISE scans, and the difficulty in visually separating short-term rapid variability from longer-term trends. We define $t_{\rm X,drop} \sim 6$ months and $t_{\rm X,incr.} \sim 3$ months, with the caveat that these may be lower limits (values up to 18–24 months are not implausible). Based on the X-ray and IR fluxes, though, it seems that by roughly late 2024, both disk and coronal luminosities had returned to the same flux levels as in ~2019–2020.

To investigate the likely mechanism(s) driving the accretion rate dip and recovery, we can review the most relevant physical timescales for an accretion disk around a $1.4 \times 10^8\,{\rm M}_\odot$ SMBH. For most CLAGN and transient events observed to date, the associated timescales of the event are usually not compatible with the viscous timescale for a geometrically thin disk (scale height $H/R \ll 1$), on the order of millennia or longer, nor with the light-crossing time. The Keplerian orbital timescale is $t_{\rm Kepl} = 2\pi[r^3/(GM_{\rm BH})]^{1/2}$. The thermal timescale is $t_{\rm th} = 1/(\alpha)[r^3/(GM_{\rm BH})]^{1/2}$, where α is the local effective viscosity parameter. The viscous accretion timescale is $t_{\rm visc} = t_{\rm th}(H/R)^{-2}$, and approaches $t_{\rm th}$ only as H/R approaches 1.

We consider the timescales in the annulus from $R \sim 30\,R_{\rm g}$ to $\sim 100\,R_{\rm g}$, the respective expected flux-weighted radii of far-UV and optical thermal continuum emission in the disk, using Eq. 1 of Edelson et al. (2019). The Keplerian timescales $t_{\rm Kepl}$ in this region range from 8 to 50 d, somewhat shorter than $t_{\rm X,drop}$ and $t_{\rm X,incr.}$. For the thermal timescales, however, arbitrarily chosen values of $\alpha \sim 0.01$–0.04 yield values of $t_{\rm th}$ of order 120–150 d, similar to $t_{\rm X,drop}$ and $t_{\rm X,incr.}$. These values of α are roughly consistent with the range (~0.01–0.1) expected based on various simulations of accretion disks (King et al. 2007), for instance where disks are supported by magnetic pressure (Jiang et al. 2019) and where MRI-induced turbulence drives angular momentum transport (Simon et al. 2012; Ju et al. 2017). However, exact values of α can depend on magnetization strength and field geometry, for example (e.g., whether vertical components exist; Hawley et al. 1995; Ju et al. 2017). For all choices of α, within these broad ranges, values of $t_{\rm th}$ (and $t_{\rm visc}$ for a geometrically thick disk) in the region of the inner accretion disk where optical/UV continuum emission peaks seem most relevant, as is the case with many changing-look and flaring AGN (e.g., Krishnan et al. 2024).

Below we consider some candidate driving mechanisms in an attempt to explain the behavior in $\dot{m}_{\rm Edd}$ and the observed multiband continuum variability:

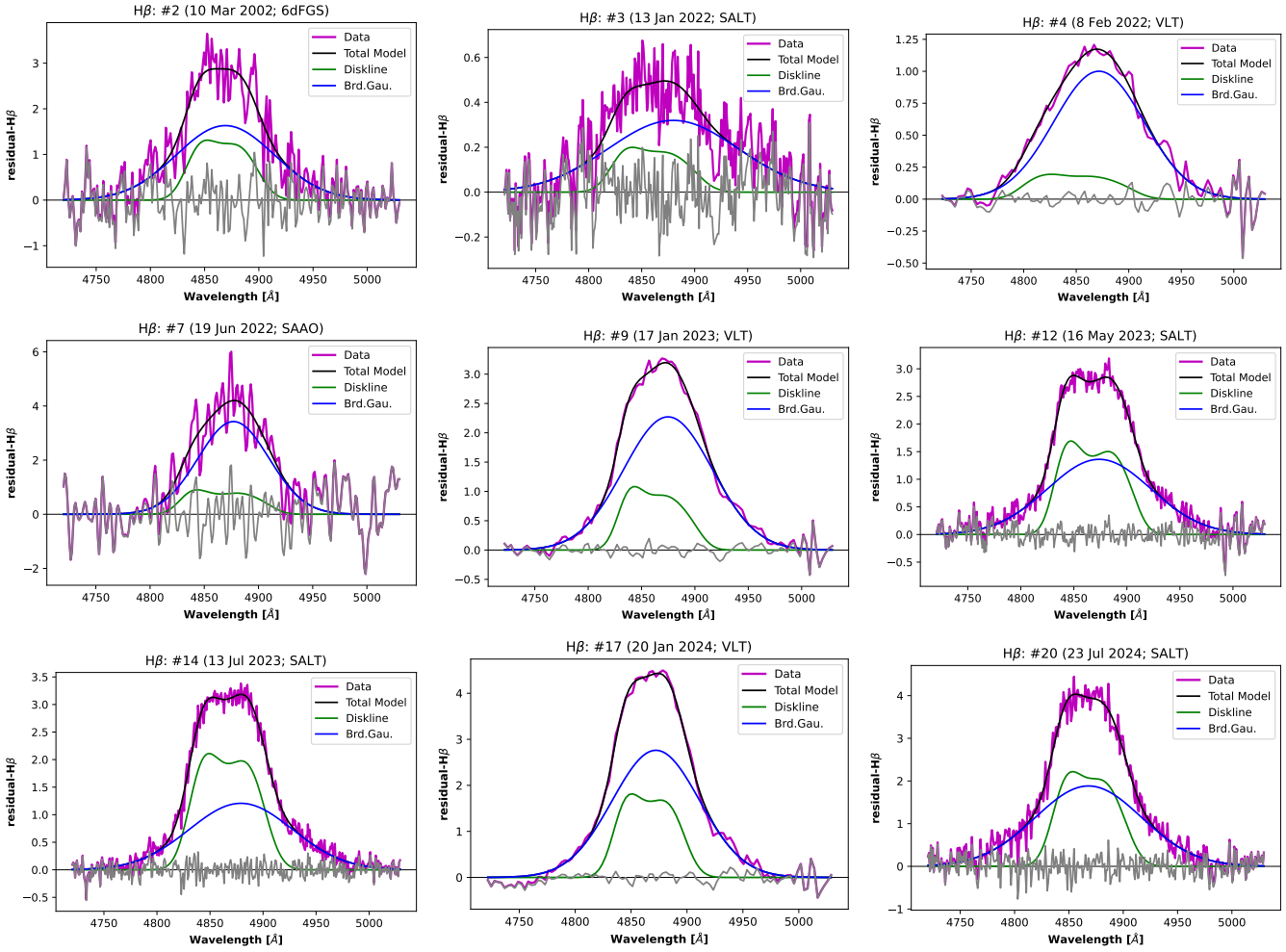

Fig. 7. Decomposition of diskline plus Gaussian components for fits to the Hβ profiles of selected optical spectra. The data (after subtraction of continuum components and [O III] lines) are shown in purple; green, blue, and black denote the diskline component, the broad Gaussian component, and the total model respectively. The Y-axis units are 10^{-16} erg cm^{-2} s^{-1} Å^{-1}.

– 1) The first possibility is a mechanism that could temporarily increase the local accretion timescale in the optical- and UV-emitting regions of the inner disk by temporarily reducing disk scale height H/R. As one example, if the accretion disk scale height is supported by magnetic pressure (Dexter & Begelman 2019), some mechanism could act to temporarily decrease that pressure.
Another possibility is that the drop and recovery in $\dot{m}_{\rm Edd}$ were caused by, respectively, a propagating cold front and warm front within the disk. Such fronts were invoked by Ross et al. (2018) to explain a 20-year flux dip and recovery in a z=0.38 quasar. The cold (warm) front would decrease (increase) H/R locally as it propagates. The front propagation timescale can be written as $t_{\rm front} \sim t_{\rm th}/(H/R)$ (Ross et al. 2018).
For r = 30 $R_{\rm g}$, arbitrary values of $(H/R) \sim 0.05$ and $\alpha \sim 0.05 - 0.10$ can yield values of $t_{\rm front}$ of 0.8 – 1.5 years, although for these same values, $t_{\rm front}$ would be a factor of 6 longer near 100 $R_{\rm g}$. Ideally, there could be an optical/UV lag that could indicate the front propagation speed and direction, but our data are insufficient to detect or constrain such a lag. As the cold front causing the luminosity dip reaches the UV-producing region of the inner disk, the reduction in seed photons from the disk reduces the Comptonized X-ray emission in both the hot and warm coronae. Another speculative possibility is that if heating the hot and/or warm coronae is facilitated by magnetic fields, then the cold front might also disrupt these fields, reducing the luminosity output of the coronae. The low value of $t_{\rm X,incr.}$ could thus be influenced by the time for the coronae to reconstitute itself. However, our data preclude any constraints on time lags between optical/UV and X-ray bands (since the UV did not clearly capture the point of lowest UV flux), so the exact sequence of events remains speculative.
– 2) A second possibility is a temporary local (impacting at least the radii of peak optical to far-UV emission) decrease, then increase, in viscosity parameter α, perhaps driven by changes in magnetic stress.
– 3) There could be a strong stochastic variation in the local mass supply. Inwardly propagating variations in local mass accretion rate have been used to explain continuum variability in Seyfert AGN across a wide range of timescales (Lyubarskii 1997; Arévalo & Uttley 2006; Ingram & Done 2011). However, the change in X-ray flux over an 18-month timescale is greater here than for most (90%) Seyfert 1 galaxies in the *Rossi X-ray Timing Explorer* archive (e.g., Markowitz & Edelson 2004) likely categorizing the variability event in J1240–2309 as an outlier.
– 4) There could be an outflowing wind, such as a magnetically driven wind (Feng et al. 2021), which can remove some

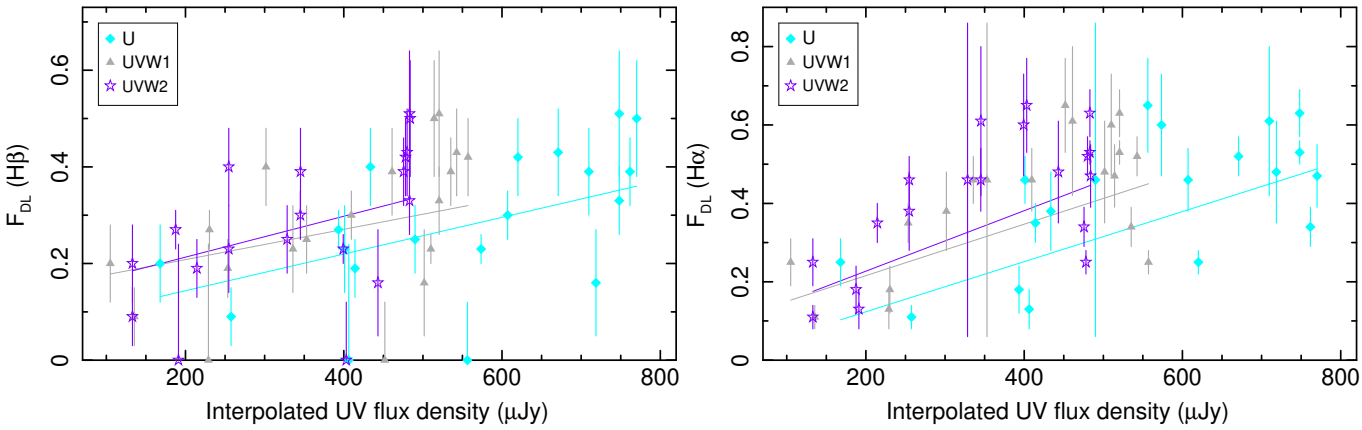

Fig. 8. $F_{\rm DL}$, the ratio of diskline component intensity to total broad-line intensity for the Hβ line (left panel) and Hα line (right panel), as a function of UV flux density, interpolated to match the dates when the optical spectra were taken. Cyan, gray, and purple denote U, UVW1, and UVW2 flux densities, respectively. The solid lines indicate the best-fitting linear relations, meant to guide the eye. Positive correlations occur in all bands for both Hβ and Hα, indicating a link between UV continuum emission and the broad Balmer profiles.

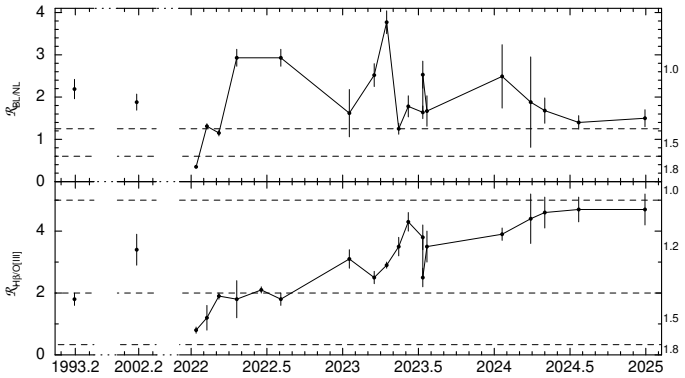

Fig. 9. $\mathcal{R}_{\rm BL/NL}$ (top panel) and $\mathcal{R}_{\rm H\beta/[O\,III]}$ (bottom panel) as a function of time. The horizontal dashed lines denote subtype classification boundaries following Runco et al. (2016, top panel) and Winkler (1992, bottom panel).

angular momentum from the disk. It is conjecturally possible that there had been such a wind in J1240–2309 whose temporary suspension decreased the removal of angular momentum, thus increasing the inflow timescale. However, this situation is somewhat speculative and contrived as we have no evidence (e.g., from X-ray spectroscopy) for such an outflow.

As a final note, we consider flux ratios taken from the SEDs that use *XMM-Newton* data, hereafter XM2/XM1 and XM3/XM1, and listed in Table B.10. We note that the soft X-ray band typically varies more than the hard band by a factor of 1.5–1.9. In addition, we note that the normalization of the CompTT component increases by factors of 2.5–3.4 faster than the normalization of the hard X-ray power-law component (Table 1). These values support the notion that the warm corona can be driven by something other than the hot corona. The accretion disk is a likely candidate, given previously observed strong correlations between these two components in persistently accreting AGN such as Mkn 509 (e.g., Mehdipour et al. 2011). However, it is also interesting to note that in J1240–2309 the warm corona flux is also more variable than the UV bands, qualitatively similar to behavior observed in the CLAGN Mkn 1018 (Saha et al. 2025a). Unlike Mkn 1018, J1240–2309 likely did not transition to an ADAF (see above). Nonetheless, the extreme variations in warm corona output suggest significant changes in the energetics and/or structure of J1240–2309's warm corona, such as radial expansion in the context of the FAGNSED model (Hagen et al. 2024). There could also be a large amount of heating at the photosphere of the disk (Palit et al. 2024); as one possibility, in magnetically dominated disks, a rising magnetic dynamo could generate such heating (Gronkiewicz et al. 2023).

There are other potential mechanisms that seem disfavored for J1240–2309 given the multiband variability behavior observed:

- A magnetic inversion in a magnetically arrested disk, following Scepi et al. (2021): An advection event travels inward, increasing UV/optical luminosity, and then temporarily destabilizing the X-ray corona, which is powered by magnetic fields via the Blandford-Znajek effect. However, this scenario predicts a sequence of variability events different to that observed here. It predicts a rise in UV/optical flux occurring well before the X-ray dip; no such rise is evident from the ATLAS or *WISE/NEOWISE* light curves. The scenario also predicts that after the X-ray dip, disk luminosity gradually decreases, not increases as observed in J1240–2309.
- Radiation-pressure (Lightman & Eardley 1974; Śniegowska et al. 2020) or hydrogen-ionization (Noda & Done 2018) instabilities: Either of these two mechanisms can operate in the accretion disk and generate heating fronts that temporarily increase H/R. However, such mechanisms are typically invoked to explain luminosity flares driven by the temporary increases in local accretion rate in black hole X-ray binaries or changing-look/flaring AGN (Krishnan et al. 2024; Saha et al. 2025b). The predicted light curve profiles (e.g., Śniegowska et al. 2020, 2023) do not resemble the flux dip displayed here.
- A switch to a radiatively inefficient (RIAF) or advection-dominated accretion flow (ADAF; e.g., Narayan & Yi 1994; Narayan et al. 1998) in the inner disk: The value of $\dot{m}_{\rm Edd}$ during the dip is indeed near the critical value below which such accretion structures can form in both stellar-mass and supermassive BHs (e.g., Yang et al. 2015, and references therein; see also Saha et al. 2025a for the CLAGN Mkn 1018). However, if a viscous geometrically thin disk switches to an RIAF/ADAF flow, then UV/optical emission should be suppressed by several orders of magnitude (Narayan et al. 1998; Abramowicz et al. 2002; Abramowicz & Fragile 2013, with

supporting observational evidence in quasars by Hagen et al. 2024). In J1240–2309, the optical/UV varies by less than the X-rays do, at least during the flux recovery. In addition, it is not clear that such a transformation out to ∼100 R_g can occur on a timescale of only six months to a year for a 10^8 $M_\odot$ black hole.

– An impact by a secondary body, such as the debris from a tidally disrupted star: Such impacts onto the inner regions of accretion disks of AGN have been invoked to explain the behavior in several CLAGN and transient AGN (e.g., Blanchard et al. (2017) and Ricci et al. (2020)). The impact creates shocks that remove angular momentum in the inner disk interior to the impact point, rapidly depleting it (e.g., Chan et al. 2019), and disrupting the processes that support the corona (Ricci et al. 2020). However, during such events, kinetic energy from the impacting debris leads to a large amount of energy dissipation and increased optical/UV radiation in the disk, although a substantial fraction of that radiation can be trapped in the disk and advected into the black hole (Chan et al. 2019).

7.3. The origins and evolution of the broad Balmer emission components in J1240–2309

Broad Hβ in local Seyferts can display shifts between being dominated by single- or double-peaked on timescales of years. One prominent example is that of NGC 5548 (e.g., Shapovalova et al. 2009), whose broad Hβ profile can display major changes on timescales of 1–2 years. Its profile is sometimes dominated by a single Gaussian, other times by a double-peaked diskline-like profile, and the relative intensities of the double peaks can vary. Another example is that of the CLAGN Mkn 1018: Lu et al. (2025) report that Balmer profiles are single-peaked toward higher values of $\dot{m}_{\rm Edd}$, when the source is subtype 1.0–1.2, and double-peaked toward lower values of $\dot{m}_{\rm Edd}$, when the source is subtype 1.5–1.8, qualitatively consistent with the observations of Elitzur et al. (2014) for samples of Seyferts. In addition, distinct kinematic regions are inferred from the broad Balmer profile shape and/or variability characteristics of some Seyferts (e.g., Shapovalova et al. 2009; Hu et al. 2020). These distinct BLR structures can sometimes be linked to other individual accretion structures, such as the inner dusty torus or a disk-like component (Nagoshi et al. 2024). Anistropic illumination of ionizing radiation onto the BLR may also yield distinct BLR regions with different dynamics and radial locations, for example (Wang et al. 2014).

The broad Hβ Gaussian component in J1240–2309 is consistent with gas located at a radial distance of 27±3 lt-dy (Sect. 6.3); the symmetry of this component supports the notion that the gas is virialized. The best-fitting models yielded mild redshifts for the peak wavelengths of both Hβ and Hα of 600–800 km s^{-1} across all spectra (including the archival spectrum). It is a strong possibility that nonvirial, infall motion can contribute to the kinematics of the BLR, as inferred from velocity-resolved reverberation studies of some Seyferts and quasars (e.g., Grier et al. 2013; Pancoast et al. 2014; Du et al. 2016; Bao et al. 2022).

Meanwhile, J1240–2309's broad Balmer profiles additionally contain a double-peaked profile. Double-peaked line profiles are also not uncommon to observe (e.g., Eracleous & Halpern 1994, 2003; Gaskell & Snedden 1999), particularly in type 1.8–1.9 Seyferts (Elitzur et al. 2014), and with variability in profile shapes and/or peak heights occurring on timescales of years (Shapovalova et al. 2004; Lewis et al. 2010). These components can often be modeled as a diskline from a static, flattened, annulus-like geometry (Chen et al. 1989; Eracleous et al. 1995) as we have done for J1240–2309. As a reminder, our best-fitting model yielded an inner radius of 600–1500 R_g = 5–12 lt-dy, with an outer radius of 5000 R_g (41 lt-dy) assumed. The inferred radial distances of the diskline and broad Gaussian are commensurate; however, it is unclear whether the two components are physically distinct or connected.

A flattened, annulus-like geometrical structure is also possible in a failed radiatively accelerated dusty outflow (FRADO; Czerny & Hryniewicz 2011), in which dusty clouds are launched from the disk, and are driven by radiation pressure acting on the dust. The BLR geometry is thus determined by the aggregate of clouds and their trajectories (Naddaf et al. 2021). It is quite intriguing to note that a radius of 5–12 lt-dy is consistent with the annulus in the disk where dusty outflows can be generated (Czerny & Hryniewicz 2011): Using Eq. 1 of Edelson et al. (2019), and assuming $\log(\dot{m}_{\rm Edd}) = -1.6$, $T = 1000$ K occurs at a radius of 9 lt-dy. Naddaf & Czerny (2022) demonstrated that emission from FRADOs can yield double- or single-peaked broad Balmer emission profiles depending on the system parameters. For instance, for a given black hole mass of 10^8 $M_\odot$, diskline-like distributions of clouds having relatively low scale heights can be preferentially generated toward values of $\log(\dot{m}_{\rm Edd}) \sim -1$ to –2, depending on the metallicity, and yielding double-peaked Balmer profiles. This range in $\dot{m}_{\rm Edd}$ overlaps with the values we infer from SED fits, supporting the notion that the diskline component is present during all timescales and accretion rates sampled during our campaign.

7.3.1. Evaluating whether the BLR components intrinsically vanished during the flux dip

Our multiband monitoring tracked J1240–2309 as $\log(\dot{m}_{\rm Edd})$ climbed from −2.4 during the flux dip to −1.6. This range overlaps well with the distributions of $\log(\dot{m}_{\rm Edd})$ recorded for several samples of changing-look AGN and quasars, which generally peak around values of $\log(\dot{m}_{\rm Edd})$ roughly −2.2 to −1.5 (e.g., Green et al. 2022; Panda & Śniegowska 2024; Zeltyn et al. 2024).

As mentioned in the Introduction, there is evidence to support the disappearance of the BLR when the accretion rate drops below a critical value, either in a statistical sense (Elitzur & Ho 2009) or in individual changing-look quasars (Green et al. 2022; Panda & Śniegowska 2024). As suggested by Elitzur & Ho (2009), if the BLR is a wind fed by the accretion disk, then accretion below the critical value means the supply of gas from the disk into the BLR is insufficient to sustain that wind. Elitzur & Ho (2009) estimated that the critical value of bolometric luminosity $L_{\rm Bol,crit}$ is 5×10^{39} $(M_{\rm BH} / 10^7\ M_\odot)^{2/3}$ erg s^{-1}. In the case of J1240–2309, given $M_{\rm BH} = 1.4 \times 10^8$ $M_\odot$, the resulting critical value for $L_{\rm Bol}$ is 3×10^{40} erg s^{-1}. However, from the SED fit to XM1, we estimate $L_{\rm Bol}$ to be 6.4×10^{43} erg s^{-1} during the flux dip, safely above the expected critical value. The observed spectral type changes, and the inferred BLR activity in J1240–2309 thus do not seem connected to the notion of the presence or lack of the BLR having a dependence on $\dot{m}_{\rm Edd}$, i.e., we did not observe that J1240–2309 became a type 2 during its low-flux state.

7.3.2. Explaining the evolution in diskline component emission

We now discuss the observed evolution in fractional contribution of the diskline component's flux to the total broad profile flux,

parameterized via $F_{\rm DL}$. In the context of the FRADO model, we can consider whether the increase in $F_{\rm DL}$ could be due to an increase in covering factor as dusty gas rises upward. The FRADO simulations of (Naddaf & Czerny 2022) indicate that for a $\sim 10^8$ $M_\odot$ BH with an accretion rate relative to Eddington of $\log(\dot{m}_{\rm Edd}) \sim -1.5$, BLR clouds may reach heights of order 50 $R_{\rm g}$ (5.5×10^9 km). In the simplest most optimistic scenario, gas can uplift vertically from the disk at a velocity $\lesssim$100 km s^{-1} for an accretion rate of $\log(\dot{m}_{\rm Edd}) = -1.5$ (Naddaf et al. 2021). Over a timescale of 1–1.5 years, gas can travel a distance of order 3×10^9 km, so such a scenario is optimistically plausible for J1240–2309. However, simulations of FRADOs so far have not considered the effects of sudden changes in luminosity. It is thus not clear if a two-year decline in bolometric luminosity is sufficient to allow clouds to fall back toward the disk faster than they are generated, thus enabling a low scale height for clouds by the time of the low-X-ray flux state.

An alternate explanation for the evolution in $F_{\rm DL}$ is that the BLR components remain dynamically static while the >13.6 eV illumination intercepted from the coronae evolves. We note that the coronae are not the only source of ionizing photons, but we consider here the potential impact of coronal evolution on the inner BLR. We consider that the double-peaked BLR component originates in a vertically and radially static diskline-like geometry with a low scale height just above the surface of the accretion disk. As the source luminosity increases, the physical extent of warm and/or hot coronae, each a source of >13.6 eV ionizing continuum emission, could increase. For instance, the scale height of the hard X-ray corona in the lamppost geometry could increase, as could the scale height or radial extent (Hagen et al. 2024) of a vertically extended warm corona as modeled in Partington et al. (2024); the major changes in warm corona luminosity observed could qualitatively support this notion. Alternately, the scale height of the inner disk itself could increase as radiation pressure increases. Such structural changes are feasible on timescales of ~1–2 years, which is longer than dynamical timescales for the innermost accretion disk. Finally, the disk may contain a warp or its surface may not be completely smooth. As a consequence of any of these possibilities, the fraction of total ionizing photons emitted by the hard corona and particularly the warm corona intercepted by the diskline component can increase as total luminosity and the scale heights of the innermost disk and/or coronae increase. Meanwhile, there can be a vertically extended BLR component that yields the broad Gaussian, but it intercepts ionizing photons in both low- and high-flux states with a static covering fraction as seen from the coronae.

A final possible explanation for the evolution in $F_{\rm DL}$ is an obscuring wind launched from the inner disk, interior to the diskline component of the BLR, and which filters the >13.6 eV continuum emission traveling from the coronae to the diskline (Dehghanian et al. 2019) only during the low-flux state. Such a wind could be launched and driven by magnetocentrifugal processes and radiation driving (e.g., Proga 2000; Proga et al. 2000; Everett 2005). However, such a scenario may be contrived given that the geometry of the wind would have to be such that it does not impact the line of sight from the coronae to the region of the BLR producing the broad Gaussian (e.g., the wind has a lower scale height than the gas producing the broad Gaussian emission component) and not intersecting the line of sight from the coronae to us, so as to avoid X-ray obscuration. Such a wind would have to be prominent during the low-flux state only, and then later dissipate, or have its number density drop below $\sim 10^{11-12}$ cm^{-3} such that it no longer absorbs >13.6 eV photons (Dehghanian et al. 2019). However, it is not clear what mechanism could cause such a wind to be launched and/or be sufficiently dense only in the low-flux state, so this scenario does not seem likely.

8. Conclusions

This paper contributes to eROSITA's window into time-domain astrophysics studies of a variety of accretion channels powering extragalactic nuclear transient events (e.g., Malyali et al. 2021; Grotova et al. 2025; Baldini et al. 2025), including X-ray detections of changing-look AGN, namely those undergoing major changes in $\dot{m}_{\rm Edd}$ (Homan et al. 2023; Krishnan et al. 2024; Saha et al. 2025b) and those undergoing changes in line-of-sight obscuration (Markowitz et al. 2024). It also highlights the utility of multiwavelength photometric and spectroscopic follow-up programs in constraining the behavior of the X-ray corona, accretion disk, and BLR during such changing-look events.

eROSITA detected a drop in soft X-ray (0.5–2 keV) flux in the $z = 0.096$ Seyfert J1240–2309 by a factor of 17 over 18 months, from June 2020 to January 2022; this dip was accompanied by a ~2-year decrease in IR flux as tracked with *NEOWISE*, with the recorded minima of both bands occurring in early 2022. Our three-year follow-up campaign tracked how the X-ray flux recovered within only 3 months, while the optical, UV, and IR bands all recovered more slowly, over ~3 years; $\dot{m}_{\rm Edd}$ increased by a factor of 7 during this time. One possible explanation for the drop and recovery in $\dot{m}_{\rm Edd}$ is the propagation of cool and warm fronts across the optical/UV continuum emitting regions of the accretion disk, as described in Ross et al. (2018). However, our campaign's optical/UV sampling was too sparse to thoroughly test this hypothesis via detection of interband lags or leads. If such fronts are relevant for explaining the behavior of other CLAGN, then we encourage future optical/UV monitoring campaigns to adopt a high cadence (e.g., a few days) to better test and constrain this class of models.

J1240–2309 also displays strong evolution in both the strength and profile shape of its broad Balmer emission lines. The broad Hβ line dropped by a factor of roughly 4–6 from March 2002 (Sy 1.0, using the Runco et al. 2016 classification) to January 2022 (Sy 1.8), during the continuum dip. The broad Hβ flux subsequently recovered by the same factor through late 2024, regaining subtype 1.0 status within a few months after the continuum dip.

We deconvolved the broad Hβ and Hα profiles into two kinematic components. A broad Gaussian, with velocity widths σ typically 1800–3900 km s^{-1} (30–50 Å), dominated the spectra taken during the first six months after the continuum dip (January 2022 – June 2022); it is consistent with virialized gas at a radial distance of 27±3 lt-dy. The second component is double-peaked, and becomes more prominent in the total broad Balmer profiles starting one year after the continuum dip. It can be modeled as a diskline (flat annulus) with an inner radius of ~1000 $R_{\rm g}$, or 5 lt-dy. The fractional contribution of the diskline to the total profile, $F_{\rm DL}$, increases as UV flux and $\dot{m}_{\rm Edd}$ increase during our campaign. One possible explanation is that the diskline component has a low scale height, but as $\dot{m}_{\rm Edd}$ increases, there is an increase in the scale height and/or radial extent of the hot and/or in particular the warm X-ray-emitting coronae; the extreme variations in warm corona luminosity that we observe could qualitatively support this notion. This increase allows a larger fraction of >13.6 eV photons to be intercepted by the diskline component. One can speculate if the increase in scale height may be connected to the putative warm propagating front that may drive the increase in $\dot{m}_{\rm Edd}$. In the context of such propagating fronts,

this change in scale height could provide a physical mechanism linking the change in accretion rate with the evolution in BLR illumination.

It is curious to note that these inferences about the geometry and location of the BLR components in J1240–2309 differ from what Nagoshi et al. (2024) concluded for the two-component BLR in the changing-state quasar SDSS J125809.31+351943.0. That object's broad Hβ profile was also decomposed into a single- and double-peaked component. However, its single-peaked BLR component is responsive to continuum variations, and inferred to be located at distances commensurate with the dusty torus; meanwhile, the stable diskline component is inferred to be associated with the outer accretion disk. This divergence in implied BLR geometries likely reflects a diversity in individual kinematic components across changing-look Seyferts and quasars. We hope that future high-cadence, multiwavelength observations of changing-look Seyferts and quasars can uncover, in addition to evidence for structural evolution in the inner disk, additional multicomponent BLRs, and take advantage of strong and rapid flux variability to study their individual components.

Acknowledgements. AM and TS acknowledge partial or full support from Narodowe Centrum Nauki (NCN) grants 2016/23/B/ST9/03123 and 2018/31/G/ST9/03224. AM also acknowledges partial support from NCN grant 2019/35/B/ST9/03944. DH acknowledges support from DLR grant FKZ 50 OR 2003. MK is supported by DFG grant KR 3338/4-1. SH is partly supported by the German Science Foundation (DFG grant numbers WI 1860/14-1 and 434448349). DAHB acknowledges support from the National Research Foundation. AM thanks Dr. Gergely Hajdu for assistance in planning LCOGT observations, and Prof. Włodzimierz Kluźniak and Dr. Debora Lančová for useful discussions on accretion disk properties. This work is based on data from eROSITA, the soft X-ray instrument aboard SRG, a joint Russian-German science mission supported by the Russian Space Agency (Roskosmos), in the interests of the Russian Academy of Sciences represented by its Space Research Institute (IKI), and the Deutsches Zentrum für Luft- und Raumfahrt (DLR). The SRG spacecraft was built by Lavochkin Association (NPOL) and its subcontractors, and is operated by NPOL with support from the Max Planck Institute for Extraterrestrial Physics (MPE). The development and construction of the eROSITA X-ray instrument was led by MPE, with contributions from the Dr. Karl Remeis Observatory Bamberg & ECAP (FAU Erlangen-Nuernberg), the University of Hamburg Observatory, the Leibniz Institute for Astrophysics Potsdam (AIP), and the Institute for Astronomy and Astrophysics of the University of Tübingen, with the support of DLR and the Max Planck Society. The Argelander Institute for Astronomy of the University of Bonn and the Ludwig Maximilians Universität Munich also participated in the science preparation for eROSITA. The eROSITA data shown here were processed using the eSASS software system developed by the German eROSITA consortium. Based on observations obtained with XMM-Newton, an ESA science mission with instruments and contributions directly funded by ESA Member States and NASA. The authors thank the *XMM-Newton* director for approving the DDT observations, and the *XMM-Newton* operations team for executing them. This research has made use of data and/or software provided by the High Energy Astrophysics Science Archive Research Center (HEASARC), which is a service of the Astrophysics Science Division at NASA/GSFC. This research has made use of the XRT Data Analysis Software (XRTDAS) developed under the responsibility of the ASI Science Data Center (ASDC), Italy. Part of this work is based on archival data, software or online services provided by the Space Science Data Center - ASI. This work was supported in part by NASA through the NICER mission and the Astrophysics Explorers Program. NICER data used in this work were gathered under a Guest Observer (GO) approved programme. Some of the observations reported in this paper were obtained with the Southern African Large Telescope (SALT) under programme 2021-2-LSP-001 for transients (PI: Buckley), conducted within the eROSITA M.O.U. as part of the eROSITA-SALT Transient collaboration, as well as under programmes 2021-2-MLT-003, 2023-1-MLT-001, and 2024-1-MLT-002 (PI: Markowitz). Polish participation in SALT is funded by grant No. MEiN nr 2021/WK/01. This paper uses observations made using the South African Astronomical Observatory (SAAO). The ATLAS science products have been made possible through the contributions of the University of Hawaii Institute for Astronomy, the Queen's University Belfast, the Space Telescope Science Institute, the South African Astronomical Observatory, and The Millennium Institute of Astrophysics (MAS), Chile. This work makes use of observations from the Las Cumbres Observatory global telescope network. This publication makes use of data products from the Wide-field Infrared Survey Explorer, which is a joint project of the University of California, Los Angeles, and the Jet Propulsion Laboratory/California Institute of Technology, funded by the National Aeronautics and Space Administration. This publication also makes use of data products from NEOWISE, which is a project of the Jet Propulsion Laboratory/California Institute of Technology, funded by the Planetary Science Division of the National Aeronautics and Space Administration. This research has made use of the NASA/IPAC Extragalactic Database (NED), which is funded by the National Aeronautics and Space Administration and operated by the California Institute of Technology. The Skynet Robotic Telescope Network is supported by the National Science Foundation, the Department of Defense, the North Carolina Space Grant Consortium, and the Mount Cuba Astronomical Foundation. This work has made use of data from the European Space Agency (ESA) mission *Gaia* (https://www.cosmos.esa.int/gaia), processed by the *Gaia* Data Processing and Analysis Consortium (DPAC, https://www.cosmos.esa.int/web/gaia/dpac/consortium). Funding for the DPAC has been provided by national institutions, in particular the institutions participating in the *Gaia* Multilateral Agreement. This research has made use of ISIS functions (ISISscripts) provided by ECAP/Remeis observatory and MIT (http://www.sternwarte.uni-erlangen.de/isis/).

References

Abramowicz, M. A. & Fragile, P. C. 2013, Living Reviews in Relativity, 16, 1
Abramowicz, M. A., Igumenshchev, I. V., Quataert, E., & Narayan, R. 2002, ApJ, 565, 1101
Akaike, H. 1973, Information Theory and an Extension of the Maximum Likelihood Principle (New York, NY: Springer New York), 199–213
Appenzeller, I., Fricke, K., Fürtig, W., et al. 1998, The Messenger, 94, 1
Arévalo, P. & Uttley, P. 2006, MNRAS, 367, 801
Arnaud, K. A. 1996, in Astronomical Society of the Pacific Conference Series, Vol. 101, Astronomical Data Analysis Software and Systems V, ed. G. H. Jacoby & J. Barnes, 17
Assef, R. J., Stern, D., Noirot, G., et al. 2018, ApJS, 234, 23
Baldini, P., Rau, A., Arcodia, R., et al. 2025, A&A, 701, A224
Bao, D.-W., Brotherton, M. S., Du, P., et al. 2022, ApJS, 262, 14
Bentz, M. C., Denney, K. D., Grier, C. J., et al. 2013, ApJ, 767, 149
Bentz, M. C., Peterson, B. M., Netzer, H., Pogge, R. W., & Vestergaard, M. 2009, ApJ, 697, 160
Blanchard, P. K., Nicholl, M., Berger, E., et al. 2017, ApJ, 843, 106
Brown, T. M., Baliber, N., Bianco, F. B., et al. 2013, PASP, 125, 1031
Bruhweiler, F. & Verner, E. 2008, ApJ, 675, 83
Brunner, H., Liu, T., Lamer, G., et al. 2022, A&A, 661, A1
Buchner, J., Brightman, M., Nandra, K., Nikutta, R., & Bauer, F. E. 2019, A&A, 629, A16
Burgh, E. B., Nordsieck, K. H., Kobulnicky, H. A., et al. 2003, in Society of Photo-Optical Instrumentation Engineers (SPIE) Conference Series, Vol. 4841, Instrument Design and Performance for Optical/Infrared Ground-based Telescopes, ed. M. Iye & A. F. M. Moorwood, 1463–1471
Burrows, D. N., Hill, J. E., Nousek, J. A., et al. 2005, Space Sci. Rev., 120, 165
Chan, C.-H., Piran, T., Krolik, J. H., & Saban, D. 2019, ApJ, 881, 113
Chen, K., Halpern, J. P., & Filippenko, A. V. 1989, ApJ, 339, 742
Cohen, R. D. 1983, ApJ, 273, 489
Crause, L. A., Gilbank, D., Gend, C. v., et al. 2019, Journal of Astronomical Telescopes, Instruments, and Systems, 5, 024007
Czerny, B. & Hryniewicz, K. 2011, A&A, 525, L8
Dauser, T., Garcia, J., Parker, M. L., Fabian, A. C., & Wilms, J. 2014, MNRAS, 444, L100
Dehghanian, M., Ferland, G. J., Peterson, B. M., et al. 2019, ApJ, 882, L30
Denney, K. D., De Rosa, G., Croxall, K., et al. 2014, ApJ, 796, 134
Dexter, J. & Begelman, M. C. 2019, MNRAS, 483, L17
Du, P., Lu, K.-X., Hu, C., et al. 2016, ApJ, 820, 27
Duras, F., Bongiorno, A., Ricci, F., et al. 2020, A&A, 636, A73
Edelson, R., Gelbord, J., Cackett, E., et al. 2019, ApJ, 870, 123
Elitzur, M. & Ho, L. C. 2009, ApJ, 701, L91
Elitzur, M., Ho, L. C., & Trump, J. R. 2014, MNRAS, 438, 3340
Eracleous, M. & Halpern, J. P. 1994, ApJS, 90, 1
Eracleous, M. & Halpern, J. P. 2003, ApJ, 599, 886
Eracleous, M., Livio, M., Halpern, J. P., & Storchi-Bergmann, T. 1995, ApJ, 438, 610
Everett, J. E. 2005, ApJ, 631, 689
Fausnaugh, M. M. 2017, PASP, 129, 024007
Feng, J., Cao, X., Li, J.-w., & Gu, W.-M. 2021, ApJ, 916, 61
Fitzpatrick, E. L. 1999, PASP, 111, 63
Frederick, S., Gezari, S., Graham, M. J., et al. 2021, ApJ, 920, 56
Freudling, W., Romaniello, M., Bramich, D. M., et al. 2013, A&A, 559, A96

Gaia Collaboration. 2022, VizieR Online Data Catalog: Gaia DR3 Part 6. Performance verification (Gaia Collaboration, 2022), VizieR On-line Data Catalog: I/360. Originally published in: 2023A&A...674A...1G
Gaia Collaboration, Prusti, T., de Bruijne, J. H. J., et al. 2016, A&A, 595, A1
Gaia Collaboration, Vallenari, A., Brown, A. G. A., et al. 2023, A&A, 674, A1
García, J., Dauser, T., Lohfink, A., et al. 2014, ApJ, 782, 76
Gaskell, C. M. & Harrington, P. Z. 2018, MNRAS, 478, 1660
Gaskell, C. M. & Snedden, S. A. 1999, in Astronomical Society of the Pacific Conference Series, Vol. 175, Structure and Kinematics of Quasar Broad Line Regions, ed. C. M. Gaskell, W. N. Brandt, M. Dietrich, D. Dultzin-Hacyan, & M. Eracleous, 157–162
Gaspari, M., Ruszkowski, M., & Oh, S. P. 2013, MNRAS, 432, 3401
Gehrels, N., Chincarini, G., Giommi, P., et al. 2004, ApJ, 611, 1005
Gendreau, K. C., Arzoumanian, Z., Adkins, P. W., et al. 2016, in Society of Photo-Optical Instrumentation Engineers (SPIE) Conference Series, Vol. 9905, Space Telescopes and Instrumentation 2016: Ultraviolet to Gamma Ray, ed. J.-W. A. den Herder, T. Takahashi, & M. Bautz, 99051H
Goodman, J. & Weare, J. 2010, Communications in Applied Mathematics and Computational Science, 5, 65
Goodrich, R. W. 1995, ApJ, 440, 141
Graham, M. J., Ross, N. P., Stern, D., et al. 2020, MNRAS, 491, 4925
Green, P. J., Pulgarin-Duque, L., Anderson, S. F., et al. 2022, ApJ, 933, 180
Grier, C. J., Peterson, B. M., Horne, K., et al. 2013, ApJ, 764, 47
Gronkiewicz, D., Różańska, A., Petrucci, P.-O., & Belmont, R. 2023, A&A, 675, A198
Grotova, I., Rau, A., Baldini, P., et al. 2025, A&A, 697, A159
Hagen, S. & Done, C. 2023, MNRAS, 521, 251
Hagen, S., Done, C., Silverman, J. D., et al. 2024, MNRAS, 534, 2803
Hawley, J. F., Gammie, C. F., & Balbus, S. A. 1995, ApJ, 440, 742
Homan, D., Krumpe, M., Markowitz, A., et al. 2023, A&A, 672, A167
Hu, C., Li, S.-S., Guo, W.-J., et al. 2020, ApJ, 905, 75
Ingram, A. & Done, C. 2011, MNRAS, 415, 2323
Jansen, F., Lumb, D., Altieri, B., et al. 2001, A&A, 365, L1
Jiang, Y.-F., Blaes, O., Stone, J. M., & Davis, S. W. 2019, ApJ, 885, 144
Jones, D. H., Read, M. A., Saunders, W., et al. 2009, MNRAS, 399, 683
Ju, W., Stone, J. M., & Zhu, Z. 2017, ApJ, 841, 29
Khachikian, E. Y. & Weedman, D. W. 1974, ApJ, 192, 581
Kilerci Eser, E., Vestergaard, M., Peterson, B. M., Denney, K. D., & Bentz, M. C. 2015, ApJ, 801, 8
King, A. R., Pringle, J. E., & Livio, M. 2007, MNRAS, 376, 1740
Kobulnicky, H. A., Nordsieck, K. H., Burgh, E. B., et al. 2003, in Society of Photo-Optical Instrumentation Engineers (SPIE) Conference Series, Vol. 4841, Instrument Design and Performance for Optical/Infrared Ground-based Telescopes, ed. M. Iye & A. F. M. Moorwood, 1634–1644
Korista, K. T. & Goad, M. R. 2000, ApJ, 536, 284
Kovačević, J., Popović, L. Č., & Dimitrijević, M. S. 2010, ApJS, 189, 15
Krishnan, S., Markowitz, A. G., Krumpe, M., et al. 2024, A&A, 691, A102
Kubota, A. & Done, C. 2018, MNRAS, 480, 1247
LaMassa, S. M., Cales, S., Moran, E. C., et al. 2015, ApJ, 800, 144
Laor, A. & Netzer, H. 1989, MNRAS, 238, 897
Leung, G. C. K., Coil, A. L., Aird, J., et al. 2019, ApJ, 886, 11
Lewis, K. T., Eracleous, M., & Storchi-Bergmann, T. 2010, ApJS, 187, 416
Lightman, A. P. & Eardley, D. M. 1974, ApJ, 187, L1
López-Navas, E., Martínez-Aldama, M. L., Bernal, S., et al. 2022, MNRAS, 513, L57
López-Navas, E., Sánchez-Sáez, P., Arévalo, P., et al. 2023, MNRAS, 524, 188
Lu, K.-X., Li, Y.-R., Wu, Q., et al. 2025, ApJS, 276, 51
Lyubarskii, Y. E. 1997, MNRAS, 292, 679
MacLeod, C. L., Green, P. J., Anderson, S. F., et al. 2019, ApJ, 874, 8
Mainzer, A., Bauer, J., Cutri, R. M., et al. 2014, ApJ, 792, 30
Malyali, A., Rau, A., Merloni, A., et al. 2021, A&A, 647, A9
Markowitz, A. & Edelson, R. 2004, ApJ, 617, 939
Markowitz, A., Krumpe, M., Homan, D., et al. 2024, A&A, 684, A101
Martin, J. R., Reichart, D. E., Dutton, D. A., et al. 2019, ApJS, 240, 12
Mason, K. O., Breeveld, A., Much, R., et al. 2001, A&A, 365, L36
McElroy, R. E., Husemann, B., Croom, S. M., et al. 2016, A&A, 593, L8
Mehdipour, M., Branduardi-Raymont, G., Kaastra, J. S., et al. 2011, A&A, 534, A39
Mejía-Restrepo, J. E., Lira, P., Netzer, H., Trakhtenbrot, B., & Capellupo, D. M. 2018, Nature Astronomy, 2, 63
Merloni, A., Lamer, G., Liu, T., et al. 2024, A&A, 682, A34
Mushotzky, R. F., Done, C., & Pounds, K. A. 1993, ARA&A, 31, 717
Naddaf, M. H. & Czerny, B. 2022, A&A, 663, A77
Naddaf, M.-H., Czerny, B., & Szczerba, R. 2021, ApJ, 920, 30
Nagoshi, S., Iwamuro, F., Yamada, S., et al. 2024, MNRAS, 529, 393
Narayan, R., Mahadevan, R., & Quataert, E. 1998, in Theory of Black Hole Accretion Disks, ed. M. A. Abramowicz, G. Björnsson, & J. E. Pringle, 148–182
Narayan, R. & Yi, I. 1994, ApJ, 428, L13
Newville, M., Stensitzki, T., Allen, D. B., & Ingargiola, A. 2014, LMFIT: Non-Linear Least-Square Minimization and Curve-Fitting for Python, Zenodo
Noda, H. & Done, C. 2018, MNRAS, 480, 3898
Osterbrock, D. E. 1977, ApJ, 215, 733
Osterbrock, D. E. 1981, ApJ, 249, 462
Osterbrock, D. E. & Koski, A. T. 1976, MNRAS, 176, 61P
Palit, B., Różańska, A., Petrucci, P. O., et al. 2024, A&A, 690, A308
Pancoast, A., Brewer, B. J., Treu, T., et al. 2014, MNRAS, 445, 3073
Panda, S. & Śniegowska, M. 2024, ApJS, 272, 13
Partington, E. R., Cackett, E. M., Edelson, R., et al. 2024, ApJ, 977, 77
Peterson, B. M., Wanders, I., Horne, K., et al. 1998, PASP, 110, 660
Petrucci, P. O., Ursini, F., De Rosa, A., et al. 2018, A&A, 611, A59
Polletta, M., Tajer, M., Maraschi, L., et al. 2007, ApJ, 663, 81
Porquet, D., Reeves, J. N., Matt, G., et al. 2018, A&A, 609, A42
Predehl, P., Andritschke, R., Arefiev, V., et al. 2021, A&A, 647, A1
Proga, D. 2000, ApJ, 538, 684
Proga, D., Stone, J. M., & Kallman, T. R. 2000, ApJ, 543, 686
Reimers, D., Koehler, T., & Wisotzki, L. 1996, A&AS, 115, 235
Ricci, C., Kara, E., Loewenstein, M., et al. 2020, ApJ, 898, L1
Ricci, C., Trakhtenbrot, B., Koss, M. J., et al. 2017, Nature, 549, 488
Ross, N. P., Ford, K. E. S., Graham, M., et al. 2018, MNRAS, 480, 4468
Ross, N. P., Graham, M. J., Calderone, G., et al. 2020, MNRAS, 498, 2339
Runco, J. N., Cosens, M., Bennert, V. N., et al. 2016, ApJ, 821, 33
Runnoe, J. C., Cales, S., Ruan, J. J., et al. 2016, MNRAS, 455, 1691
Saha, T., Krumpe, M., Markowitz, A., et al. 2025a, A&A, 699, A205
Saha, T., Markowitz, A., Homan, D., et al. 2025b, A&A, 702, A28
Salvato, M., Wolf, J., Dwelly, T., et al. 2025, A&A, 704, A344
Sánchez-Sáez, P., Lira, H., Martí, L., et al. 2021, AJ, 162, 206
Saxton, R. D., Motta, S. E., Komossa, S., & Read, A. M. 2015, MNRAS, 454, 2798
Scepi, N., Begelman, M. C., & Dexter, J. 2021, MNRAS, 502, L50
Schawinski, K., Koss, M., Berney, S., & Sartori, L. F. 2015, MNRAS, 451, 2517
Schlegel, D. J., Finkbeiner, D. P., & Davis, M. 1998, ApJ, 500, 525
Schmidt, E. O., Oio, G. A., Ferreiro, D., Vega, L., & Weidmann, W. 2018, A&A, 615, A13
Shapovalova, A. I., Doroshenko, V. T., Bochkarev, N. G., et al. 2004, A&A, 422, 925
Shapovalova, A. I., Popović, L. Č., Bochkarev, N. G., et al. 2009, New A Rev., 53, 191
Shappee, B. J., Prieto, J. L., Grupe, D., et al. 2014, ApJ, 788, 48
Shen, Y. 2021, ApJ, 921, 70
Sheng, Z., Wang, T., Jiang, N., et al. 2020, ApJ, 889, 46
Sheng, Z., Wang, T., Jiang, N., et al. 2017, ApJ, 846, L7
Simon, J. B., Beckwith, K., & Armitage, P. J. 2012, MNRAS, 422, 2685
Smith, K. W., Smartt, S. J., Young, D. R., et al. 2020, PASP, 132, 085002
Śniegowska, M., Czerny, B., Bon, E., & Bon, N. 2020, A&A, 641, A167
Śniegowska, M., Grzędzielski, M., Czerny, B., & Janiuk, A. 2023, A&A, 672, A19
Sołtan, A. 1982, MNRAS, 200, 115
Stern, D., Assef, R. J., Benford, D. J., et al. 2012, ApJ, 753, 30
Stern, D., McKernan, B., Graham, M. J., et al. 2018, ApJ, 864, 27
Strüder, L., Briel, U., Dennerl, K., et al. 2001, A&A, 365, L18
Suberlak, K. L., Ivezić, Ž., & MacLeod, C. 2021, ApJ, 907, 96
Sugiura, N. 1978, Communications in Statistics-theory and Methods, 7, 13
Sunyaev, R., Arefiev, V., Babyshkin, V., et al. 2021, A&A, 656, A132
Titarchuk, L. 1994, ApJ, 434, 570
Tohline, J. E. & Osterbrock, D. E. 1976, ApJ, 210, L117
Tonry, J. L., Denneau, L., Heinze, A. N., et al. 2018, PASP, 130, 064505
Trakhtenbrot, B., Arcavi, I., MacLeod, C. L., et al. 2019, ApJ, 883, 94
van Groningen, E. & Wanders, I. 1992, PASP, 104, 700
Vestergaard, M. & Peterson, B. M. 2006, ApJ, 641, 689
Wang, J.-M., Qiu, J., Du, P., & Ho, L. C. 2014, ApJ, 797, 65
Wang, S., Woo, J.-H., Gallo, E., et al. 2024, ApJ, 966, 128
Wang, T. G., Zhou, H. Y., Grupe, D., et al. 2009, AJ, 137, 4002
White, R. J. & Peterson, B. M. 1994, PASP, 106, 879
Willingale, R., Starling, R. L. C., Beardmore, A. P., Tanvir, N. R., & O'Brien, P. T. 2013, MNRAS, 431, 394
Wilms, J., Allen, A., & McCray, R. 2000, ApJ, 542, 914
Winkler, H. 1992, MNRAS, 257, 677
Wright, E. L. 2006, PASP, 118, 1711
Wright, E. L., Eisenhardt, P. R. M., Mainzer, A. K., et al. 2010, AJ, 140, 1868
Wu, J., Wu, Q., Xue, H., Lei, W., & Lyu, B. 2023, ApJ, 950, 106
Yang, Q., Green, P. J., Wu, X.-B., et al. 2025, ApJ, 980, 91
Yang, Q., Wu, X.-B., Fan, X., et al. 2018, ApJ, 862, 109
Yang, Q.-X., Xie, F.-G., Yuan, F., et al. 2015, MNRAS, 447, 1692
Zeltyn, G., Trakhtenbrot, B., Eracleous, M., et al. 2022, ApJ, 939, L16
Zeltyn, G., Trakhtenbrot, B., Eracleous, M., et al. 2024, ApJ, 966, 85

Appendix A: Summary of X-ray, optical/UV, and optical spectroscopic observations

Below, we list observation logs summarizing the X-ray observations (Table A.1), the optical/UV space- and ground-based photometric observations (Table A.2), and the optical spectroscopic observations (Table A.3).

Appendix B: Additional details on observations and data reduction

All *XMM-Newton*, eROSITA/eRASS, and *Swift* reductions were performed using HEASOFT v. 6.32.1 software.

B.1. eROSITA/eRASS reduction

All eROSITA/eRASS data were extracted using event processing version c020 and eSASS version 21121_0_4 (Brunner et al. 2022). We combined data from all seven telescope modules (TMs). We extracted counts for J1240–2309 using a circular extraction region with the radius scaled to the 0.2–2.3 keV maximum likelihood (ML) count rate from the eRASS source catalog; that is, the extraction regions have larger radii corresponding to higher count rates. ML count rates take into account the time when the source was in the field of view, and with corrections for vignetting effects applied. Similarly, background regions were extracted using annuli whose inner and outer radii depend on ML count rate, and with excising point sources detected in the background extraction region, again using circular regions whose radii depended on ML count rate. Extraction radii, vignetting-corrected exposure times, and ML count rates are listed in Table B.1.

B.2. XMM-Newton EPIC reduction

We observed J1240–2309 with *XMM-Newton* on 25–26 January 2022 (XM1; revolution 4052) for a net duration of 55 ks, on 26 January 2023 (XM2; revolution 4236) for 15 ks, and on 22 January 2025 (XM3; revolution 4601) for 41 ks, using both the EPIC pn and MOS cameras each time. For XM1, all EPIC cameras were operated in Full Frame mode. For XM2, when the source was brighter, the pn was in Small Window mode, while both MOS cameras were in Large Window mode. For XM3, all three cameras were in Large Window mode. The medium optical blocking filter was used in all cases. We reduced the data using XMM Science Analysis Software (XMMSAS) version 21.0, following standard extraction procedures for point sources. Source spectra were extracted from circles 40″ in radius; background spectra were extracted from source-free regions with the same size located a few arcminutes away and on the same CCD chip. We screened data against strong, time-localized background flares due to proton flux by filtering on the 5–13 keV background rate. For XM1, six flares totaling 17 ks were excised; for XM2, three short flares totaling 2 ks were excised; for XM3, the first ∼10 ks were excised. For the pn, we selected data from pattern 0 and pattern 1–4 separately (pn0 and pn14 throughout this paper) due to their slightly different energy resolutions and due to potential calibration issues between patterns 0 and 1–4 in Small Window mode. We checked for pileup using the XMM-SAS task EPATPLOT but found no evidence for any pileup. Good time exposures after screening are listed in Table A.1. The numbers of spectral counts for XM1 are 3659, 1213, 1446, and 1520 for 0.25–10 keV pn0, 0.5–10 keV pn14, 0.2–10 keV MOS1, and 0.2–10 keV MOS2, respectively; for XM2, the corresponding spectral counts are 6534, 1922, 2894, and 2951, respectively; for XM3, values are 26251, 7382, 9672, and 9132, respectively.

B.3. Swift XRT reduction

Swift performed 15 observations of J1240–2309, as listed in Table A.1. We examined XRT photon counting (PC) mode data. We reprocessed raw event files using XRTPIPELINE version 0.13.7 and the latest XRT calibration files. We extracted source spectra using circular regions of radius 20 pixels (47″); background spectra were extracted from annular regions of inner radius 40 pixels (94″) and outer radius 80 pixels (188″), and confirmed to be free of background sources. We generated ancillary response files using XRTMKARF, and we selected the PC mode response files from the calibration database. Good exposure times after screening are listed in Table A.1.

B.4. NICER

We used NICERDAS version 11a software, and followed standard procedures to screen data, produce cleaned event files, and extract spectra. We discarded data from detectors 14 and 34, which are prone to excessive noise. We rejected time intervals when the detector undershoot rate[11] exceeded 150 ct s^{-1} per module. We also screened out time intervals when the detector overshoot rate (caused when high-energy particles deposit excess charge) exceeded 1.5 ct s^{-1}. Given the source faintness, we discarded data taken during the ISS' passage through the South Atlantic Anomaly (SAA) boundary, which is defined to be more conservative and cover a slightly larger area than for the standard NICERSAA boundary. We used the 3C50 background estimation method, screening out times where the background rate in the hard band (13–15 keV) exceeded 0.5 ct s^{-1} in the hard band. As noted in Sect. 4.2, we summed all 28 observations to maximize the signal-to-noise ratio. Given the danger of underestimated optical loading impacting the softest energies, and given the faintness of the source, we discarded data below 0.4 keV and above 4 keV.

B.5. XMM-Newton OM reduction

During XM1, the Optical Monitor (OM) aboard *XMM-Newton* observed J1240–2309 with one exposure each at V, B, and U bands, two exposures at UVW1, and six exposures for M2, with each exposure lasting 4.4 ks. During XM2, one exposure was obtained at each of V, B, U, UVW1, and UVM2 bands, with each exposure lasting 2.2 ks. All exposures were taken in image mode + fast mode.

We reduced the data using the XMM_SAS routines OMICHAIN and OMFCHAIN for the image and fast modes, respectively. These routines apply flat-fielding, source detection, and aperture photometry for each exposure, and they combine all exposure images into a mosaiced image, and perform source detection and aperture photometry on the mosaiced image. The source extraction radius was 12 pixels = 5.″7. These routines also correct fluxes for detector dead time. We verified that the source was well detected within each exposure, that there were no obvious imaging artifacts in any exposure. The resulting flux densities are listed in Table B.2. To generate spectral files, we used the SAS tool OM2PHA.

[11] Detector undershoots are reset events that occur when incoming photons trigger a cascade of accumulate charge.

Table A.1. X-ray observation log of J1240–2309

Telescope	ObsID	Date	Date (MJD)	Exposure (ks)	Abbr.
XMM EPIC	(slew)	1 Jan. 2013	56293.9	0.008	
eROSITA/eRASS1		29–31 Dec. 2019	58847.5	0.14	eR1
eROSITA/eRASS2		29–30 Jun. 2020	59029.6	0.11	eR2
eROSITA/eRASS3		30–31 Dec. 2020	59213.9	0.11	eR3
eROSITA/eRASS4		2–3 Jul. 2021	59398.3	0.12	eR4
eROSITA/eRASS5		3–4 Jan. 2022	59583.3	0.12	eR5
XMM EPIC	0862770901	25–26 Jan. 2022	59604.9	32.4, 36.9, 36.9	XM1
Swift XRT	00015025001	23 Feb. 2022	59633.3	2.7	Sw1
Swift XRT	00015025002	29 March 2022	59667.7	2.9	Sw2
Swift XRT	00015025003	26 Jul. 2022	59786.3	1.7	Sw3
Swift XRT	00015440001	21 Dec. 2022	59934.3	4.4	Sw4
XMM EPIC	0903991901	26 Jan. 2023	59970.2	8.3, 11.7, 11.7	XM2
NICER	(see Appdx. B.4)	15 Feb. 2023 – 23 May 2023	59990–60087	48.5	N ICER
Swift XRT	00015025004	22 Mar. 2023	60025.5	1.9	Sw5
Swift XRT	00016018001	14 May 2023	60078.6	2.8	Sw6
Swift XRT	00016142001	23 Jul. 2023	60148.4	2.1	Sw7
Swift XRT	00016142002	26 Jul. 2023	60151.6	0.9	Sw8
Swift XRT	00016409001	6 Dec. 2023	60284.3	1.6	Sw9
Swift XRT	00016409002	10 Dec. 2023	60288.1	1.4	Sw10
Swift XRT	00097539001	26 Apr. 2024	60426.7	0.5	Sw11
Swift XRT	00097539002	1 Aug. 2024	60523.3	0.6	Sw12
Swift XRT	00097539003	5 Aug. 2024	60527.0	0.2	Sw13
Swift XRT	00097539004	22 Aug. 2024	60544.7	2.1	Sw14
Swift XRT	00097539005	25 Aug. 2024	60547.1	0.9	Sw15
XMM EPIC	0903992001	22 Jan. 2025	60697.4	28.1, 29.9, 30.0	XM3

Notes. All MJD dates refer to the midpoint of the observation. Exposure refers to good time after screening. For eRASS, exposure times have been corrected for vignetting. For *XMM-Newton*, the three exposure values refer to pn, MOS1, and MOS2, respectively. For NICER, there were 28 observations from 15 February 2023 (MJD 59990) to 23 May 2023 (MJD 60087); we combined all observations for spectral analysis, and here we list the summed exposure. The NICER exposure-weighted MJD midpoint was 60034.4.

In order to combine these flux densities with those from *Swift* UVOT purely for the purpose of creating a combined light curve, it is neccesary to account for the slight offsets in effective wavelengths between UVOT and OM. We estimated local spectral slopes from the SED via simple linear interpolations, and we estimated the flux densities at the effective wavelengths of the corresponding UVOT filter.

We also examined the flux densities of two nearby stars, Gaia DR3 3501932993890436224 and 3501932169256712448, located 0.′7 to the north and 1.′2 to the east, respectively. For both stars, flux densities are consistent with being constant to within their uncertainties at all bands, indicating a lack of significant systematic uncertainty.[12] Again, we estimated local spectral slopes from the SED, and estimated flux densities at the effective wavelengths of the corresponding UVOT filter (discussed in §B.6).

B.6. Swift UVOT reduction

We performed aperture photometry using the ftool UVOTSOURCE. We extracted source spectra using circular regions of radius 6″. Background spectra were extracted using annular regions, free of nearby point sources, with inner and outer radii 17.″5 and 25″, respectively. We obtained flux densities for J1240–2309 as well as for the same two stars considered in the OM observations. We confirmed that in both stars, flux densities are consistent with being constant in all filters both for the UVOT-only light curves and the combined OM+UVOT light curves, indicating that the variability measured in J1240–2309 is real and intrinsic to the AGN. Magnitudes and flux densities for J1240–2309 are listed in Table B.3. Finally, we used the Ftool UVOTSOURCE to generate source and background spectral files, using the same source and background extraction regions as for the aperture photometry.

[12] Systematic corrections based on the stellar light curves were thus not applied to the target.

B.7. LCOGT photometry

The nine ground-based photometric observations of J1240–2309 were obtained using Sinistro 1-meter telescopes operated by the Las Cumbres Observatory global telescope network from March 2022 to May 2023 (LCO1–9). LCO1–4 and 6–9 each used Johnson-Cousins/Bessell I-, R-, V-, and B-band filters, with two exposures of 90 s for I, two exposures of 120 s for V, two exposures of 120 s for R, and two exposures of 180 s for B; LCO5 used the V and B filters with exposures of 60 s and 80 s, respectively. LCOGT data are automatically processed using the

Table A.2. Optical/UV photometric observations of J1240–2309

Observation & Instrument	Date	Date (MJD)	Filters	Exposure (s)
XMM-Newton OM (XM1)	25–26 Jan. 2022	59604.9	V, B, U, UVW1, UVM2	4400, 4400, 4400, 8800, 26400
PROMPT-6 (P1)	6 Feb. 2022	59616.4	B	600
PROMPT-6 (P2)	7 Feb. 2022	59617.4	V, B	600, 600
PROMPT-6 (P3)	9 Feb. 2022	59619.4	B	600
PROMPT-6 (P4)	11 Feb. 2022	59621.4	V, B	600, 600
PROMPT-6 (P5)	12 Feb. 2022	59622.4	V	600
PROMPT-6 (P6)	13 Feb. 2022	59623.4	R	600
PROMPT-6 (P7)	19 Feb. 2022	59629.1	R, V, B	600, 600, 600
Swift UVOT (Sw1)	23 Feb. 2022	59633.3	V, B, U, UVW1, UVM2, UVW2	138, 138, 138, 415, 1085, 691
PROMPT-6 (P8)	23 Feb. 2022	59633.1	R, V, B	600, 600, 600
PROMPT-6 (P9)	28 Feb. 2022	59638.3	R, V, B	600, 600, 600
LCOGT/LSC (LCO1)	1 Mar. 2022	59639.3	I, R, V, B	180, 240, 240, 360
PROMPT-6 (P10)	11 Mar. 2022	59649.1	R, V, B	600, 600, 600
PROMPT-6 (P11)	20 Mar. 2022	59658.1	R, V, B	600, 600, 600
PROMPT-6 (P12)	27 Mar. 2022	59665.3	R, V, B	600, 600, 600
Swift UVOT (Sw2)	29 Mar. 2022	59667.7	V, B, U, UVW1, UVM2, UVW2	148, 148, 148, 446, 1210, 746
PROMPT-6 (P13)	7 May 2022	59706.1	R, V, B	600, 600,600
LCOGT/LSC (LCO2)	5 May 2022	59704.2	I, R, V, B	180, 240, 240, 360
LCOGT/LSC (LCO3)	13 Jun. 2022	59743.0	I, R, V, B	180, 240, 240, 360
LCOGT/CPT (LCO4)	13 Jul. 2022	59773.8	I, R, V, B	180, 240, 240, 360
Swift UVOT (Sw3)	26 Jul. 2022	59786.3	V, B, U, UVW1, UVM2, UVW2	139, 139, 139, 276, 417, 553
Swift UVOT (Sw4)	21 Dec. 2022	59934.3	V, B, U, UVW1, UVM2, UVW2	368, 368, 368, 739, 933, 1480
LCOGT/CPT (LCO5)	29 Dec. 2022	59942.0	V, B	60, 80
LCOGT/LSC (LCO6)	5 Jan. 2023	59949.3	I, R, V, B	180, 240, 240, 360
XMM-Newton OM (XM2)	26 Jan. 2023	59970.2	V, B, U, UVW1, UVM2	2200, 2200, 2200, 2200, 2200
LCOGT/COJ (LCO7)	16 Feb. 2023	59991.7	I, R, V, B	180, 240, 240, 360
LCOGT/LSC (LCO8)	22 Mar. 2023	60025.1	I, R, V, B	180, 240, 240, 360
Swift UVOT (Sw5)	22 Mar. 2023	60025.5	UVW1, UVM2, UVW2	567, 637, 637
Swift UVOT (Sw6)	14 May 2023	60078.6	UVW1, UVM2, UVW2	832, 951, 951
LCOGT/LSC (LCO9)	24 May 2023	60088.2	I, R, V, B	180, 240, 240, 360
Swift UVOT (Sw7)	23 Jul. 2023	60148.4	V, B, U, UVW1, UVM2, UVW2	164, 169, 205, 411, 440, 655
Swift UVOT (Sw8)	26 Jul. 2023	60151.6	V, B, U, UVW1, UVM2, UVW2	76, 76, 76, 153, 182, 307
Swift UVOT (Sw9)	6 Dec. 2023	60284.3	V, B, U, UVW1, UVM2, UVW2	125, 125, 125, 251, 96, 162
Swift UVOT (Sw10)	10 Dec. 2023	60288.1	V, B, U, UVW1, UVM2, UVW2	113, 113, 113, 226, 322, 454
Swift UVOT (Sw11)	26 Apr. 2024	60426.7	V, U, UVW1, UVM2, UVW2	86, 86, 86, 86, 86
Swift UVOT (Sw12)	1 Aug. 2024	60523.3	V, B, U, UVW1, UVM2, UVW2	101, 82, 101, 101, 101, 101
Swift UVOT (Sw13)	5 Aug. 2024	60527.0	V, B, U, UVW1, UVM2, UVW2	57, 48, 57, 57, 51, 57
Swift UVOT (Sw14)	22 Aug. 2024	60544.7	V, B, U, UVW1, UVM2, UVW2	190, 154, 190, 190, 190, 190
Swift UVOT (Sw15)	25 Aug. 2024	60547.1	V, B, U, UVW1, UVM2, UVW2	155, 128, 155, 155, 155, 155
XMM-Newton OM (XM3)	22 Jan. 2025	60697.3	V, B, U, UVW1, UVM2, UVW2	4400, 4400, 4400, 13200, 8800, 13200

Notes. MJD date refers to the midpoint of the observation (time-average of all exposures). Exposure times are summed over all exposures for a given filter. LCOGT/LSC, CPT, and COJ indicate the 1-meter telescopes at Cerro Tololo Inter-American Observatory, South African Astronomical Observatory, and Siding Spring Observatory, respectively, all operated by the Las Cumbres Observatory global telescope network.

BANZAI pipeline,[13] which performs standard calibration steps including masking bad pixels, biasing, dark subtraction, and flat fielding.

We performed aperture photometry by stacking the pairs of exposures, and extracting source-centered circles of radius 6″ and background annuli with inner and outer radii of 19″ and 26″, chosen to avoid nearby faint stars, and extracted magnitudes. We also extracted magnitudes for five reference stars located roughly 4–5′ away, GAIA DR3 3501934849316325248, GAIA DR3 3501928973801041408, GAIA DR3 3501928905081564288,

[13] https://lco.global/documentation/data/BANZAIpipeline/

Table A.3. Optical spectroscopic observations of J1240–2309

#	Telescope & Instrument	Date	MJD	Total Exposure (s)
1	H/ESO 3.6m EFOSC1	13 Mar. 1993	49059	300
2	UK Schmidt 6dF	10 Mar. 2002	52343	1200
3	SALT RSS	13 Jan. 2022	59592	600
4	VLT FORS2	8 Feb. 2022	59618	450 (300I), 750 (300V), 750 (1400V)
5	SALT RSS	9 Mar. 2022	59647	525 (Hβ), 600 (Hα)
6	SALT RSS	21 Apr. 2022	59690	630 (Hβ), 630 (Hα)
7	SAAO 1.9m	19 Jun. 2022	59749	1200
8	SAAO 1.9m	5 Aug. 2022	59796	2400
9	VLT FORS2	17 Jan. 2023	59961	450 (300I), 450 (300V), 1200 (1400V)
10	SAAO 1.9m	18 Mar. 2023	60021	2400
11	SAAO 1.9m	17 Apr. 2023	60051	2400
12	SALT RSS	16 May 2023	60080	680
13	VLT FORS2	8 Jun. 2023	60103	1020 (300I), 1020 (300V)
14	SALT RSS	13 Jul. 2023	60138	680
15	VLT FORS2	13 Jul. 2023	60138	1020 (300I), 1020 (300V)
16	SAAO 1.9m	23 Jul. 2023	60148	2400
17	VLT FORS2	20 Jan. 2024	60329	1020 (300I), 1020 (300V)
18	SALT RSS	29 Mar. 2024	60398	680
19	SALT RSS	2 May 2024	60432	700
20	SALT RSS	23 Jul. 2024	60514	700
21	SALT RSS	30 Dec. 2024	60674	700

Notes. We refer to Reimers et al. (1996) and Jones et al. (2009) for details on spectra #1 and #2, and to Appendix B.10 for details on instrumental setups for spectra #3–21.

Table B.1. eRASS extraction regions, exposure times, and ML count rates

eRASS	Source Radius (″)	Background Annulus Radii (″)	Exposure (s)	ML Count Rate (ct s^{-1}; 0.2–2.3 keV)
1	92.3	194.3, 1147.9	240	1.31 ± 0.11
2	95.0	199.1, 1180.9	113	1.45 ± 0.12
3	84.2	179.7, 1047.8	114	0.95 ± 0.10
4	74.1	161.1, 922.7	122	0.60 ± 0.08
5	37.9	91.0, 474.4	119	0.057 ± 0.024

Notes. Exposure refers to good time after screening and after correction for vignetting effects. ML count rate (Merloni et al. 2024) denotes the maximum likelihood count rate taking into account the time when the source was in the field of view, and with corrections for vignetting effects applied.

GAIA DR3 3501929076880260736, and GAIA DR3 3501932920876028544 (UCAC4 335-068176), calibrating against synthetic photometric magnitudes generated from *Gaia* DR3 (Gaia Collaboration et al. 2016, 2023) mean spectra in the performance verification catalog (Gaia Collaboration 2022). We converted magnitudes to flux densities using standard Vega magnitudes for Johnson-Cousins/Bessell filters.[14] The resulting magnitudes and flux densities are listed in Table B.4.

B.8. PROMPT-6 optical photometry

All observations were obtained with the PROMPT 6 telescope at Cerro Tololo Inter-American Observatory (CTIO), operated as part of Skynet (for details about the network, see Martin et al. 2019), and using Johnson–Cousins B, V, and R filters. For each filter, we observed the target with five 120 s exposures with a field of view of 13.′5×13.′5 arranged in a 3×3 dither pattern with a 40″ dither step, providing improved sampling of flat-field and detector inhomogeneities. The five exposures in each filter were subsequently aligned and combined and the time assigned to each stacked image corresponds to the median MJD of its individual components. Image reduction followed standard procedures, including bias subtraction, dark correction, and flat-fielding using nightly calibration frames. The dither pattern also enabled effective removal of cosmic rays and bad pixels. Observed (not corrected for Galactic reddening) Vega magnitudes are listed in Table B.8.

[14] e.g., https://www.astronomy.ohio-state.edu/martini.10/usefuldata.html

Table B.2. *XMM-Newton* OM photometric Vega magnitudes and flux density measurements

Obs.	Date (MJD)	V	B	U	UVW1	UVM2	UVW2
XM1	59604.9	16.937 ± 0.018	17.832 ± 0.015	17.404 ± 0.017	17.476 ± 0.019	17.699 ± 0.032	–
		631 ± 11	317 ± 4	168 ± 3	105 ± 2	67 ± 2	–
XM2	59970.2	16.752 ± 0.022	17.618 ± 0.015	16.526 ± 0.013	16.193 ± 0.018	16.666 ± 0.045	–
		750 ± 15	456 ± 6	378 ± 5	343 ± 6	173 ± 7	–
XM3	60697.3	16.421 ± 0.014	17.172 ± 0.008	16.095 ± 0.007	15.684 ± 0.004	15.754 ± 0.011	15.681 ± 0.016
		1017 ± 13	689 ± 5	563 ± 4	548 ± 2	400 ± 4	405 ± 6

Notes. The top value is the Vega magnitude. The bottom value is the flux density in μJy.

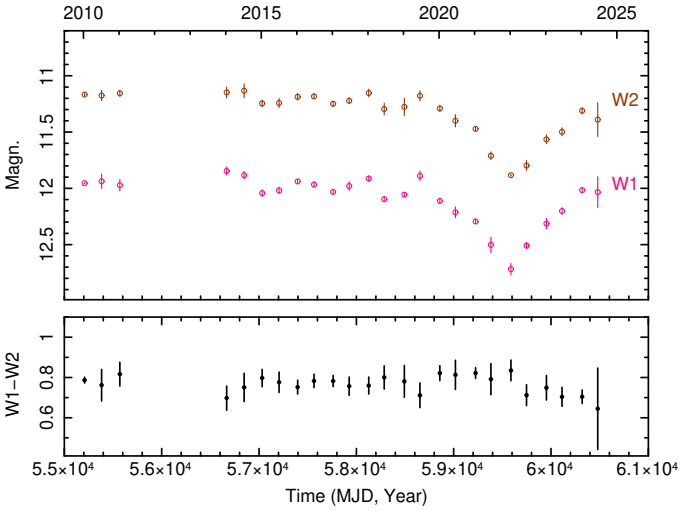

Fig. B.1. *WISE/NEOWISE* W1 and W2 band light curves, binned to 180 days (top panel). W1−W2 is plotted in the lower panel.

B.9. ATLAS and WISE/NEOWISE

To access publicly available photometry from the Asteroid Terrestrial impact Last Alert System (ATLAS; Tonry et al. 2018; Smith et al. 2020), we used ATLAS' online forced-photometry pipeline to generate o-band (orange; 560-820 nm) and c-band (cyan; 420–650 nm) light curves. We used data from 22 November 2017 (MJD 58097) to 24 December 2023 (MJD 60302), and filtered against flux density data points that were obvious outliers or had error bars larger than 25%. They are plotted in Fig. 1.

We also obtained public IR photometric monitoring courtesy of the *Widefield Infrared Survey Explorer* (*WISE*)/*NEOWISE* mission (Wright et al. 2010; Mainzer et al. 2014). We downloaded all single-epoch W1 and W2 band photometry points from the AllWISE Multiepoch Photometry Table and the NEOWISE-R Single Exposure Source Table catalogs hosted at the NASA/IPAC Infrared Science Archive (IRSA[15]), collecting data taken from 12 January 2010 (MJD 55208) until 18 June 2023 (MJD 60113). We rebinned the light curves to one flux point every six months; the resulting W1 and W2 light curves, as well as W1−W2, are plotted in Fig. B.1.

B.10. Optical spectroscopy

The VLT-FORS2 spectra were taken with a number of different instrumental setups and exposure times. All spectra presented in this work are composite spectra, formed by combining multiple observations taken in a single run. Spectra #4 and #9 are a combination of spectra taken with grism 300V (4450–8650 Å), 300I and filter OG590 (6000–11000 Å), and grism 1400V (4560–5860 Å; Hβ). The other FORS2 observations only made use of grisms 300V and 300I+OG590. We give an overview of the spectral observations in Table B.10. The slit width for all observations was 1.″3 and the seeing over the observing nights ranged from 0.″3 to 2.″2. With regard to the level of seeing, we note that the weather on all observing nights was calm, which means the upper limits of the seeing range likely represent only brief spikes during the run. For the reduction of the VLT data we made use of the `esoreflex` pipeline (Freudling et al. 2013), which conducts all standard CCD processing, as well as the spectral extraction, wavelength calibration, and the flux calibration. Arc and standard star spectra were taken on the night. FORS2 spectra #4 and #9 were taken as part of ESO programs 105.20UT and 109.23MH (PI: M. Krumpe), respectively, and spectra #13, 15, and 17 as part of program 109.22XH (PI: D. Homan).

Observations at SALT RSS used the pg0900 grating (to achieve spectral resolution approximately 800–1200), and a slit width of 1.″5. All observations used a grating angle of 16.25° (camera angle 32.5°) to cover both the Hα and Hβ regions. Observations #5 and #6 additionally used a grating angle of 13.25° (camera angle 26.5°) to sample from the Hβ region to 3200 Å. All observations used normal mode, the faint gain, and 2×2 binning. Exposure times, listed in Table A.3, were in the range 525–700 s.

Observations at SAAO used the low-resolution grating on the SpUpNIC spectrograph, with a slit width of 2.″7. Exposures were 2 × 1200 s for all observations except for spectrum #7 (19 June 2022), which had a 1 × 1200 s exposure.

All CCD data were reduced using standard bias corrections and flat-fielding. Wavelength calibration used arc-lamp spectra taken the same night. Spectrophotometric calibrations were applied using standard stars (although such calibrations were not possible for spectra #1 and 2, the archival Hamburg/ESO and 6dFGS spectra).

We cross-calibrated all optical spectra using the framework of van Groningen & Wanders (1992) and Fausnaugh (2017), which accounts for differing apertures, wavelength resolutions, slit widths, weather conditions, air masses, and absolute wavelength calibration issues by matching [O III] integrated fluxes and profile widths. Further details can be found in Saha et al. (2025b). We used spectrum #3 (SALT) as the reference spectrum, and applied flux scaling (gray-shifted) factors. Because the two archival spectra, #1 and 2, were not flux-calibrated, we must treat all continuum and absolute line fluxes as ap-

[15] https://irsa.ipac.caltech.edu

Table B.3. UVOT photometric Vega magnitudes and flux density measurements

Observation & Instrument	Date (MJD)	V	B	U	UVW1	UVM2	UVW2
Swift UVOT (Sw1)	59633.3	16.34 ± 0.12	17.20 ± 0.12	16.50 ± 0.11	16.79 ± 0.12	16.69 ± 0.10	16.86 ± 0.11
		1060 ± 110	534 ± 50	362 ± 36	171 ± 19	163 ± 11	133 ± 12
Swift UVOT (Sw2)	59667.7	16.43 ± 0.09	17.09 ± 0.09	16.29 ± 0.08	16.11 ± 0.08	16.15 ± 0.07	16.09 ± 0.07
		973 ± 78	593 ± 38	441 ± 31	320 ± 24	268 ± 12	270 ± 15
Swift UVOT (Sw3)	59786.3	16.47 ± 0.08	17.22 ± 0.08	16.39 ± 0.07	16.50 ± 0.08	16.65 ± 0.09	16.48 ± 0.07
		943 ± 67	523 ± 32	402 ± 25	223 ± 18	168 ± 10	189 ± 11
Swift UVOT (Sw4)	59934.3	16.35 ± 0.08	17.01 ± 0.07	16.22 ± 0.07	16.13 ± 0.08	16.26 ± 0.08	16.30 ± 0.07
		1050 ± 70	639 ± 34	468 ± 27	315 ± 23	241 ± 14	222 ± 13
Swift UVOT (Sw5)	60025.5	–	–	–	16.00 ± 0.10	16.01 ± 0.11	15.86 ± 0.09
		–	–	–	354 ± 34	304 ± 25	334 ± 26
Swift UVOT (Sw6)	60078.6	–	–	–	15.51 ± 0.07	15.48 ± 0.07	15.47 ± 0.06
		–	–	–	558 ± 35	496 ± 23	478 ± 25
Swift UVOT (Sw7)	60148.4	16.22 ± 0.08	16.63 ± 0.07	15.68 ± 0.06	15.60 ± 0.07	15.46 ± 0.07	15.46 ± 0.06
		1190 ± 70	906 ± 42	771 ± 41	514 ± 35	505 ± 22	484 ± 23
Swift UVOT (Sw8)	60151.6	16.34 ± 0.13	16.70 ± 0.10	15.71 ± 0.08	15.66 ± 0.10	15.56 ± 0.11	15.46 ± 0.08
		1060 ± 120	847 ± 66	753 ± 57	485 ± 45	458 ± 36	485 ± 31
Swift UVOT (Sw9)	60284.3	16.68 ± 0.18	17.16 ± 0.14	16.04 ± 0.10	16.09 ± 0.11	16.12 ± 0.12	16.12 ± 0.09
		778 ± 125	556 ± 61	554 ± 49	326 ± 34	274 ± 26	263 ± 21
Swift UVOT (Sw10)	60288.1	16.32 ± 0.09	16.84 ± 0.08	16.06 ± 0.07	16.00 ± 0.08	16.37 ± 0.09	16.02 ± 0.07
		1080 ± 80	746 ± 41	541 ± 32	355 ± 27	219 ± 13	287 ± 15
Swift UVOT (Sw11)	60426.7	16.22 ± 0.08	–	15.69 ± 0.06	15.54 ± 0.09	15.58 ± 0.11	15.46 ± 0.09
		1180 ± 80	–	765 ± 44	540 ± 46	451 ± 35	484 ± 38
Swift UVOT (Sw12)	60523.3	16.15 ± 0.08	16.78 ± 0.08	15.78 ± 0.06	15.74 ± 0.09	15.86 ± 0.11	15.87 ± 0.10
		1260 ± 80	785 ± 48	704 ± 40	453 ± 40	347 ± 29	331 ± 28
Swift UVOT (Sw13)	60527.0	16.33 ± 0.12	16.81 ± 0.10	15.86 ± 0.08	15.83 ± 0.12	16.00 ± 0.15	16.07 ± 0.13
		1070 ± 100	763 ± 60	654 ± 46	414 ± 45	307 ± 37	274 ± 31
Swift UVOT (Sw14)	60544.5	16.45 ± 0.09	16.87 ± 0.08	15.86 ± 0.06	15.86 ± 0.08	15.92 ± 0.10	15.89 ± 0.08
		957 ± 75	722 ± 40	654 ± 33	403 ± 31	329 ± 22	325 ± 23
Swift UVOT (Sw15)	60547.1	16.31 ± 0.09	16.83 ± 0.08	15.91 ± 0.06	15.99 ± 0.09	15.97 ± 0.10	15.95 ± 0.09
		1090 ± 80	753 ± 44	626 ± 35	358 ± 30	315 ± 24	309 ± 24

Notes. The top value is the Vega magnitude. The bottom value is the flux density in μJy.

Table B.4. LCOGT photometric Vega magnitudes and flux density measurements

Observation	Date (MJD)	I	R	V	B
LCO1	59639.3	15.430 ± 0.003 1624.8 ± 4.5	16.058 ± 0.007 $1155.5^{+7.5}_{-7.4}$	16.561 ± 0.003 862.8 ± 2.4	17.298 ± 0.003 $489.0^{+1.4}_{-1.3}$
LCO2	59704.2	15.364 ± 0.003 1726.6 ± 4.8	15.919 ± 0.002 1313.3 ± 2.4	16.388 ± 0.003 1011.8 ± 2.8	17.051 ± 0.004 613.9 ± 2.3
LCO3	59743.0	15.317 ± 0.004 $1803.0^{+6.7}_{-6.6}$	15.905 ± 0.003 1330.4 ± 3.7	16.368 ± 0.005 $1030.6^{+4.8}_{-4.7}$	16.926 ± 0.005 688.8 ± 3.2
LCO4	59773.8	15.408 ± 0.007 1658.0 ± 10.7	15.953 ± 0.006 $1272.8^{+7.1}_{-7.0}$	16.422 ± 0.010 $980.6^{+9.1}_{-9.0}$	17.119 ± 0.015 $576.6^{+8.0}_{-7.9}$
LCO5	59942.0			16.456 ± 0.016 $950.4^{+14.0}_{-13.9}$	17.057 ± 0.022 $610.5^{+12.5}_{-12.2}$
LCO6	59949.3	15.343 ± 0.003 1760.3 ± 4.9	15.945 ± 0.003 1282.3 ± 3.5	16.419 ± 0.004 983.3 ± 3.6	17.035 ± 0.005 623.0 ± 2.9
LCO7	59991.7	15.338 ± 0.003 1768.5 ± 4.9	15.930 ± 0.002 1300.1 ± 2.4	16.398 ± 0.002 1002.5 ± 1.8	17.013 ± 0.003 635.8 ± 1.8
LCO8	60025.1	15.269 ± 0.002 1884.5 ± 3.5	15.841 ± 0.002 1411.2 ± 2.6	16.272 ± 0.002 1125.9 ± 2.1	16.812 ± 0.002 765.1 ± 1.4
LCO9	60088.2	15.237 ± 0.002 1940.9 ± 3.6	15.788 ± 0.001 1481.8 ± 1.4	16.191 ± 0.002 1213.1 ± 2.2	16.656 ± 0.002 883.3 ± 1.6

Notes. The top value is the Vega magnitude. The bottom values are the flux densities in μJy. Values are not corrected for Galactic extinction.

proximate, although parameters based on relative line fluxes derived from lines that are very close in wavelength (e.g., $F_{\rm DL}$, $R_{\rm H\beta/[O\,III]}$, $R_{\rm BL/NL}$) are still valid, albeit with some potential additional systematic uncertainty compared to the flux-calibrated spectra. We note from Fig. 5 that spectrum #7, taken with SAAO SpUpNIC on 19 June 2022, seems to have a continuum level that is roughly 40% higher compared to other spectra taken in mid-2022, including another SpUpNIC spectrum. As plotted in Fig. 1, LCOGT photometry taken close in time (LCO3) do indicate a relatively higher optical continuum at this time. Another possibility is strong host galaxy contamination: an absorption feature near 5090 Å (rest-frame), associated with host-galaxy absorption, is somewhat strong here. Finally, we applied dereddening corrections to all spectra, using $E(B-V) = 0.057$ (Schlegel et al. 1998), R=3.1, and the Galactic extinction function of (Fitzpatrick 1999). Best-fitting parameters from our optical spectral fits (Sect. 6.1) are listed in Tables B.7, B.8, and B.9.

B.11. Energy-resolved flux ratios

For the purpose of exploring broadband variability properties as the source luminosity increases, we list in Table B.10 values of ratios of the best-fit SED models, derived in Sect. 5. We note that the soft X-ray band, dominated by contributions from the warm corona, is always the most variable band.

Table B.5. PROMPT-6 photometric Vega magnitudes

Date (MJD)	R	V	B
59616.4 (P1)	–	–	17.20 ± 0.17 535^{+91}_{-78}
59617.4 (P2)	–	16.73 ± 0.16 738^{+117}_{-101}	17.67 ± 0.20 347^{+70}_{-58}
59619.4 (P3)	–	–	17.48 ± 0.17 414^{+70}_{-60}
59621.4 (P4)	–	16.66 ± 0.17 788^{+134}_{-114}	17.48 ± 0.18 414^{+75}_{-63}
59622.4 (P5)	–	16.60 ± 0.15 832^{+123}_{-107}	–
59623.4 (P6)	16.17 ± 0.15 1042^{+154}_{-134}	–	–
59629.1 (P7)	16.13 ± 0.15 1081^{+160}_{-140}	16.67 ± 0.14 780^{+107}_{-94}	17.47 ± 0.14 417^{+57}_{-50}
59633.1 (P8)	16.11 ± 0.13 1101^{+140}_{-124}	16.62 ± 0.12 817^{+95}_{-86}	17.49 ± 0.14 410^{+56}_{-50}
59638.3 (P9)	16.10 ± 0.14 1112^{+153}_{-134}	16.61 ± 0.14 825^{+114}_{-100}	17.31 ± 0.12 484^{+57}_{-51}
59649.1 (P10)	16.12 ± 0.14 1091^{+150}_{-132}	16.60 ± 0.14 832^{+115}_{-101}	17.33 ± 0.12 475^{+55}_{-50}
59658.1 (P11)	16.07 ± 0.14 1143^{+157}_{-138}	16.56 ± 0.14 864^{+119}_{-104}	17.35 ± 0.13 466^{+59}_{-53}
59665.3 (P12)	16.04 ± 0.14 1175^{+162}_{-142}	16.50 ± 0.14 913^{+126}_{-110}	17.16 ± 0.28 555^{+163}_{-126}
59706.1 (P13)	16.00 ± 0.15 1219^{+181}_{-157}	16.46 ± 0.13 947^{+120}_{-107}	17.08 ± 0.13 598^{+76}_{-67}

Notes. The top value is the Vega magnitude. The bottom value is the flux density in μJy. These values are not corrected for Galactic extinction.

Table B.6. VLT-FORS2 instrumental setups

	Date	Setup	Exposure (s)	Seeing
4	8 Feb. 2022	300I	450	0″.4–1″.9
		300V	750	
		1400V	750	
9	17 Jan. 2023	300I	450	0″.3–2″.2
		300V	450	
		1400V	1200	
13	8 Jun. 2023	300I	1020	0″.5–1″.6
		300V	1020	
15	13 Jul. 2023	300I	1020	0″.3–0″.8
		300V	1020	
17	20 Jan. 2024	300I	1020	0″.5–2″.2
		300V	1020	

Table B.10. Ratios of SED model flux densities

	U	W1	M2	0.5 keV	4 keV
XM2/XM1	2.9	3.2	3.8	9.7	6.5
XM3/XM1	4.7	5.6	8.5	12.4	6.6

Table B.7. Best-fitting model parameters for the broad Hβ line

	Gaussian			Diskline					Total broad	
Date	λ_{cent} (Å)	σ (Å)	Flux[a]	λ_o (Å)	σ_0 (Å)	R_{in} (R_g)	Incl. i (°)	Flux[a]	line flux[a]	F_{DL}[b]
#1 H/ESO 03/93	4878±3	44±3	201±32[c]	4861*	10*	1440±520	13*	63±23[c]	264±16[c]	0.24±0.09
#2 6dF 03/02	4869±2	45±5	185±44[c]	4861*	10*	940±200	13*	88±24[c]	273±15[c]	0.32±0.12
#3 SALT 01/22	4877±4	60±6	51±11	4853±3	10±5	500±180	13*	13±5	64±4	0.20±0.08
#4 VLT 02/22	4870±2	43±11	115±9	4845±4	10*	1000*	22±4	12±8	127±4	0.09±0.06
#5 SALT 03/22	4889±48	61±4	124±14	4855±2	10*	640±110	13*	46±5	170±8	0.27±0.04
#6 SALT 04/22	4889±50	39±3	121±16	4855±2	10*	830±100	13*	83±12	204±5	0.40±0.08
#7 SAAO 06/22	4877±3	33±2	280±46	4861*	10*	660±110	13*	67±55	347±16	0.19±0.16
#8 SAAO 08/22	4874±2	37±2	274±40	4861*	10*	1000*	13*	<73	274±18	<0.24
#9 VLT 01/23	4875±1	42±1	237±21	4855±3	10±2	540±140	11±1	72±26	309±27	0.23±0.09
#10 SAAO 03/23	4877±3	56±5	247±36	4873±2	10*	920±19	13*	81±20	328±16	0.25±0.07
#11 SAAO 04/23	4868±1	33±1	327±27	4861*	10*	1000*	13*	<42	327±6	<0.12
#12 SALT 05/23	4874±1	49±2	167±16	4863±1	10±1	830±120	14±1	118±19	285±13	0.42±0.08
#13 VLT 06/23	4876±1	44±2	234±23	4861±1	10±1	840±130	13±1	178±32	412±22	0.43±0.09
#14 SALT 07/23	4879±2	49±2	147±13	4862±1	21±1	1160±230	16±1	152±36	299±12	0.51±0.13
#15 VLT 07/23	4867±4	25±1	161±9	4864±1	6±1	1220±230	18±2	79±16	240±15	0.33±0.07
#16 SAAO 07/23	4889±7	46±3	170±36	4860±1	11±2	830±80	13*	173±22	343±40	0.50±0.12
#17 VLT 01/24	4872±1	39±2	270±32	4861±1	14±2	1000*	13±1	115±13	385±21	0.30±0.05
#18 SALT 03/24	4869±1	35±1	282±24	4861±1	3±2	1000*	15±1	56±36	338±58	0.16±0.11
#19 SALT 05/24	4864±2	40±3	231±34	4867±1	14±1	1000*	13±1	149±15	380±25	0.39±0.07
#20 SALT 07/24	4868±1	49±2	229±24	4863±1	11±1	800±160	12±1	147±35	376±18	0.39±0.09
#21 SALT 12/24	4866±1	45±1	311±20	4866±1	10±2	1000*	13±1	91±8	402±22	0.23±0.03

Notes. An asterisk (*) indicates a fixed parameter.
[a]: Line flux units are 10^{-16} erg cm^{-2} s^{-1}.
[b]: F_{DL} is the fraction contribution of the flux of the diskline component to the total broad-line flux. For the diskline component, λ_o is the rest-frame wavelength of emission, σ_0 quantifies the local broadening due to electron scattering in a photoionized atmosphere, R_{in} is the inner radius, and i is the disk inclination, defined such that 0° indicates a face-on disk. The outer radius R_{out} was always held fixed at 5000 R_g.
[c]: Absolute flux calibration was not available for spectra #1 and #2; values of absolute line flux should be considered as estimates only.

Table B.8. Best-fitting model parameters for the broad Hα line

	Gaussian			Diskline					Total broad	
Date	λ_{cent} (Å)	σ (Å)	Flux[a]	λ_o (Å)	σ_0 (Å)	R_{in} (R_g)	Incl. i (°)	Flux[a]	line flux[a]	F_{DL}[b]
#2 6dF 03/02	6572±3	41±2	351±43[c]	6560±2	15*	320±190	8±3	83±76[c]	434±13[c]	0.19±0.17
#3 SALT 01/22	6557±1	55±2	166±11[c]	6548±1	10±7	1110±210	15±1	54±13[c]	220±4[c]	0.25±0.06
#4 VLT 02/22	6569±6	51±1	525±14	6544±2	8±2	600±120	10±1	63±17	589±9	0.11±0.03
#5 SALT 03/22	6560±1	47±1	297±16	6552±1	6±2	1420±390	16±2	64±19	361±5	0.18±0.06
#6 SALT 04/22	6560±1	52±3	310±51	6555±1	12±2	760±100	12±1	186±39	496±7	0.38±0.10
#7 SAAO 06/22	6575±2	53±2	793±21	6559±2	15*	1000*	11±1	425±62	1218±22	0.35±0.05
#8 SAAO 08/22	6576±1	50±1	756±48	6554±4	15*	1000*	12±1	108±41	864±18	0.13±0.05
#9 VLT 01/23	6578±1	71±1	467±18	6563±1	11±1	840±40	16±1	399±20	866±20	0.46±0.06
#10 SAAO 03/23	6589±5	51±5	483±256	6566±5	20±4	800±390	12±3	413±269	896±15	0.46±0.40
#11 SAAO 04/23	6594±1	99±4	436±37	6566±1	22±1	790±120	12±1	825±139	1261±37	0.65±0.12
#12 SALT 05/23	6577±6	49±2	475±10	6554±5	6±1	1130±80	15±1	159±15	634±13	0.25±0.03
#13 VLT 06/23	6587±2	87±3	504±35	6566±5	8±1	1100±90	18±1	542±49	1046±22	0.52±0.05
#14 SALT 07/23	6563±1	100±22	327±14	6564±4	18±1	1000±80	14±1	564±36	892±13	0.63±0.07
#15 VLT 07/23	6584±1	85±2	533±23	6566±4	11±1	1250±100	18±1	590±22	1123±16	0.53±0.03
#16 SAAO 07/23	6590±2	53±1	486±37	6564±8	11±1	1250±80	16±1	434±69	920±53	0.47±0.08
#17 VLT 01/24	6569±2	84±2	534±27	6566±1	10±1	1640±240	20±1	459±75	992±15	0.46±0.08
#18 SALT 03/24	6576±2	50±2	346±34	6562±8	9±1	$2000^{+0\dagger}_{500}$	18±2	322±125	668±40	0.48±0.13
#19 SALT 05/24	6579±1	43±6	482±23	6557±6	8±2	1390±180	16±1	243±33	725±19	0.34±0.05
#20 SALT 07/24	6585±1	72±2	329±20	6566±5	17±1	1630±290	16±1	536±169	865±17	0.61±0.19
#21 SALT 12/24	6567±3	74±2	403±20	6569±5	18±1	$2000^{+0\dagger}_{430}$	17±2	601±285	1004±18	0.60±0.13

Notes. An asterisk (*) indicates a fixed parameter.
A dagger (†) indicates parameter uncertainty pegging at a limit.
[a]: Line flux units are 10^{-16} erg cm^{-2} s^{-1}.
[b]: F_{DL} is the fraction contribution of the flux of the diskline component to the total broad-line flux. For the diskline component, λ_o is the rest-frame wavelength of emission, σ_0 quantifies the local broadening due to electron scattering in a photoionized atmosphere, R_{in} is the inner radius, and i is the disk inclination, defined such that 0° indicates a face-on disk. The outer radius R_{out} was always held fixed at 5000 R_g.
[c]: Absolute flux calibration was not available for spectra #1 and #2; values of absolute line flux should be considered as estimates only.

Table B.9. Additional best-fitting model parameters for optical spectral fits

	Hβ region						Hα region		
Date	χ^2/dof	F^a_{5100}	[O III] flux^b	$R_{H\beta/[O\,III]}$	Narrow Hβ flux^b	$R^d_{BL/NL}$	χ^2/dof	Narrow Hα flux^b	He I flux^b
#1 H/ESO 03/93	219.26/182=1.21	1.00±0.35^c	143±12^c	1.8±0.2	20±4^c	$\frac{2.80\pm0.11}{1.28\pm0.21}$ = 2.19 ± 0.23	–	–	–
#2 6dF 03/02	1271.52/820=1.55	4.56±0.36^c	81±12^c	3.4±0.5	12±3^c	$\frac{2.89\pm0.13}{1.54\pm0.36}$ = 1.88 ± 0.19	853.44/867=0.98	48±3^c	88±9^c
#3 SALT 01/22	1788.67/1268=1.41	2.81±0.08	83±3	0.8±0.1	10±1	$\frac{0.47\pm0.02}{1.31\pm0.07}$ = 0.35 ± 0.02	2524.13/1349=1.87	42±1	4±1
#4 VLT 02/22	402.44/381=1.06	1.72±0.08	108±1	1.2±0.4	11±1	$\frac{1.17\pm0.03}{0.89\pm0.06}$ = 1.31 ± 0.06	629.20/448=1.40	85±2	4±1
#5 SALT 03/22	859.40/1277=0.67	3.97±0.14	90±2	1.9±0.1	8±1	$\frac{1.31\pm0.04}{1.14\pm0.13}$ = 1.15 ± 0.07	1393.76/1349=1.03	31±1	41±5
#6 SALT 04/22	997.10/1281=0.78	2.70±0.02	112±2	1.8±0.6	6±1	$\frac{2.26\pm0.05}{0.77\pm0.14}$ = 2.93 ± 0.20	1697.43/1354=1.25	26±1	46±3
#7 SAAO 06/22	739.38/1078=0.69	9.06±0.48	165±5	2.1±0.1	<5	–^{e}	132.66/850=0.16	106±6	68±17
#8 SAAO 08/22	767.36/1073=0.72	6.96±0.43	149±9	1.8±0.2	14±4	$\frac{2.26\pm0.05}{0.77\pm0.14}$ = 2.93 ± 0.20	324.87/850=0.38	104±4	14±14
#9 VLT 01/23	543.02/368=1.48	2.27±0.21	98±2	3.1±0.3	11±2	$\frac{1.51\pm0.31}{0.93\pm0.14}$ = 1.62 ± 0.56	630.04/442=1.43	82±10	91±5
#10 SAAO 03/23	977.38/1074=0.91	7.72±0.34	131±7	2.5±0.2	17±4	$\frac{2.90\pm0.11}{1.15\pm0.24}$ = 2.52 ± 0.27	496.98/849=0.59	81±4	47±9
#11 SAAO 04/23	1331.23/1083=1.24	6.78±0.23	113±2	2.9±0.1	12±2	$\frac{3.81\pm0.07}{1.01\pm0.15}$ = 3.77 ± 0.27	703.17/843=0.83	86±3	101±11
#12 SALT 05/23	2387.77/1278=1.87	4.32±0.15	80±5	3.5±0.3	10±1	$\frac{1.83\pm0.13}{1.46\pm0.11}$ = 1.25 ± 0.13	1319.22/1345=0.98	35±1	77±3
#13 VLT 06/23	521.97/367=1.42	5.27±0.23	95±2	4.3±0.3	17±2	$\frac{2.69\pm0.20}{1.51\pm0.15}$ = 1.78 ± 0.25	604.27/445=1.36	148±10	149±8
#14 SALT 07/23	2288.66/1280=1.79	4.36±0.14	79±7	3.8±0.4	10±1	$\frac{2.17\pm0.11}{1.32\pm0.11}$ = 1.64 ± 0.15	1319.33/1346=0.98	35±1	72±3
#15 VLT 07/23	464.60/373/1.27	4.51±0.22	97±8	2.5±0.3	10±1	$\frac{2.73\pm0.12}{1.08\pm0.12}$ = 2.53 ± 0.32	760.49/443=1.72	110±10	140±7
#16 SAAO 07/23	1372.40/1059=1.30	7.76±0.58	98±10	3.5±0.5	18±4	$\frac{2.54\pm0.27}{1.52\pm0.32}$ = 1.67 ± 0.36	580.44/843=0.69	123±14	81±9
#17 VLT 01/24	667.94/373=1.82	4.77±0.24	100±2	3.9±0.2	11±3	$\frac{2.12\pm0.25}{0.85\pm0.19}$ = 2.49 ± 0.75	725.32/443=1.64	108±13	118±5
#18 SALT 03/24	833.60/1287=0.65	5.07±0.34	77±5	4.4±0.8	12±2	$\frac{3.09\pm0.89}{1.64\pm0.30}$ = 1.88 ± 1.07	1034.59/1348=0.77	32±2	94±6
#19 SALT 05/24	1157.03/1280=0.90	4.75±0.29	83±8	4.6±0.5	9±1	$\frac{2.17\pm0.21}{1.29\pm0.17}$ = 1.68 ± 0.30	1385.65/1346=1.03	44±2	109±5
#20 SALT 07/24	837.42/1277=0.66	3.49±0.24	79±6	4.7±0.4	10±1	$\frac{2.06\pm0.15}{1.47\pm0.15}$ = 1.40 ± 0.16	1023.50/1347=0.76	47±1	102±4
#21 SALT 12/24	1231.28/1267=0.97	4.64±0.29	86±8	4.7±0.5	10±1	$\frac{2.16\pm0.18}{1.44\pm0.16}$ = 1.50 ± 0.20	1157.24/1341=0.86	45±1	100±4

Notes. ^{a}: Flux densities are in units of 10^{-16} erg cm^{-2} s^{-1} Å^{-1}
^{b}: Integrated line fluxes are in units are 10^{-16} erg cm^{-2} s^{-1}
^{c}: Absolute flux calibration was not available for spectra #1 and #2; values of F_{5100} and absolute line flux should be considered as estimates only.
^{d}: Ratio of broad Hβ to narrow Hβ line peak flux density (both in units of 10^{-16} erg cm^{-2} s^{-1} Å^{-1}), following Runco et al. (2016).
^{e}: Ratio not calculated due to narrow Hβ line not being detected.